Journal of
Marine Science and Engineering

Article

Assessment of Numerical Captive Model Tests for Underwater Vehicles: The DARPA SUB-OFF Test Case

Vito Vasilis Zheku *, Diego Villa, Benedetto Piaggio, Stefano Gaggero and Michele Viviani *

Department of Electrical, Electronic, Telecommunication Engineering and Naval Architecture, University of Genova, Via All'Opera Pia, 11A, 16145 Genova, Italy; diego.villa@unige.it (D.V.); benedetto.piaggio@unige.it (B.P.); stefano.gaggero@unige.it (S.G.)

* Correspondence: vitovasil.zheku@edu.unige.it (V.V.Z.); michele.viviani@unige.it (M.V.)

Abstract: During the early design stage of an underwater vehicle, the correct assessment of its manoeuvrability is a crucial task. Conducting experimental tests still has high costs, especially when dealing with small vehicles characterized by low available budget. In the current investigation, virtual towing tank tests are simulated using the open-source OpenFOAM library in order to assess the reliability of CFD methods for the prediction of hydrodynamic forces and moments. A well-known case study, the Defence Advanced Research Projects Agency (DARPA) SUB-OFF model, is used, and the outcomes are compared to the experimental results available in the literature. Five different configurations are investigated for pure drift tests, rudder tests and pure rotation in both vertical and horizontal plane. The results show an overall good agreement with the experimental data with a quite low demanding mesh arrangement of 3M cells, a favourable balance between accuracy and computational time. In more detail, the expected error in the most significant forces during manoeuvres is less than 2% for the fully appended configuration (the submarine real operative condition), whereas the accuracy is moderately reduced for the barehull configuration (a case not representative of a real hull) with an expected error of 15%. A possible reason for the differences observed could be attributed to the description of the two streamwise vortices generated when manoeuvring. Apart from the lateral force and yaw moment, the results of the longitudinal force are also presented, having a greater disparity when compared to the experimental data. Nevertheless, the longitudinal force has no important role for the purpose of making stability and control predictions. The study contributes to the validation and consolidation of CFD methods, offering insights into their accuracy and limitations for practical applications in underwater vehicles.

Keywords: naval hydrodynamics; CFD; submarines; RANS; underwater vehicles; DARPA; manoeuvrability

Citation: Zheku, V.V.; Villa, D.; Piaggio, B.; Gaggero, S.; Viviani, M. Assessment of Numerical Captive Model Tests for Underwater Vehicles: The DARPA SUB-OFF Test Case. *J. Mar. Sci. Eng.* **2023**, *11*, 2325. https://doi.org/10.3390/jmse11122325

Academic Editors: Nastia Degiuli and Ivana Martić

Received: 6 November 2023
Revised: 29 November 2023
Accepted: 2 December 2023
Published: 8 December 2023

1. Introduction

Nowadays, more and more underwater vehicles (UVs) are being used, not only for military, but also for exploration or scientific purposes [1]. Underwater vehicles (like submarines or small crafts) are characterized by complex shapes, yet during the design stage, the correct assessment of the manoeuvrability and stability of a submarine is a crucial task. Thus, additional dedicated studies are needed. Unfortunately, the reference literature is limited, and industrial or military restrictions often limit the access to experimental data.

The main notions for studying the manoeuvrability of submarines are very similar to that of surface ships, with the main difference the increase to 6-DoF [2] and the influence of the restoring forces on the vertical plane, with crucial consequences for the vertical stability and change depth ability [3]. Often, during the design phase, to simplify the problem, the motions in 6-DoF are decoupled into the horizontal and vertical components, making the analysis simpler and enabling the separation of the main effects and aspects. As a consequence of that, it is clear that the reliable evaluation of the hydrodynamic coefficients is a crucial aspect in predicting the motion of the vehicles for manoeuvring prediction purposes.

Studies have been carried out traditionally to predict the hydrodynamic derivatives of a submarine using either empirical formulae, or captive model experiments, considering all available types of tests such as translational, rotating arm and PMM (planar motion mechanism) ones (see among others [4,5]). Fureby et al. [6] conducted an experimental and numerical study of the Defence Science and Technology Organisation (DSTO) generic submarine model in both straight-ahead conditions and a 10° side-slip in the low-speed wind tunnel at Fishermans Bend in Melbourne. Similar measurements were carried out by Anderson et al. [4] and Quick et al. [5], presenting an experimental campaign focused on generic conventional submarine hulls, testing different drift and pitch angles. These kinds of results are useful in order to compare and consolidate the use of computational fluid dynamics for the prediction of the hydrodynamic forces, and consequently the extrapolation of the hydrodynamic coefficients. Moreover, in the last decades, thanks to the growth of computational resources, CFD simulations have also been considered as a possible source of data. In the study conducted by Fureby, complementary numerical calculations were carried out, using both RANS (Reynolds-averaged Navier–Stokes equations) with the kOmegaSST formulation (kOmega shear stress transport) and LES (large eddy simulation) with two different models, the LDKM (localized dynamic kinetic energy model) and the MM (mixed model), having unstructured grids with up to 340M cells. Dubbioso et al. [7] investigated the effect of the stern appendages' configuration on the turning qualities of a fully appended notional submarine (CNR-INSEAN 2475), by means of numerical simulations, using an in-house CFD solver. Both cross-shaped and X-rudder configuration were examined, in two different operation conditions, open water and snorkeling depth. Broglia et al. [8] carried out an analysis of the vortices shed in steady drift and pitch advancement of the BB2 submarine at four operative conditions, namely straight ahead, drift, and both positive and negative pitch. Their results were compared with experiments available in the literature [9], showing the accuracy that CFD predictions can provide.

Wackers et al. [10] presented a comprehensive analysis of the KRISO (Korean Institute of Ships and Ocean Engineering) Very Large Crude Carrier no. 2 (KVLCC2) flow field, with a particular emphasis on the effects of vortices. Their paper discusses the challenges of turbulence modelling in accurately simulating these flow patterns and compares computational results with experimental measurements, shedding light on the vital role of turbulence modelling in marine flow simulations. In a study by Zhang et al. [11], the unsteady Reynolds-averaged Navier–Stokes (URANS) method was employed to simulate the surfacing motion of a submarine model (DARPA-SUBOFF) in regular waves. The outcomes showed that in the proximity of the free surface, underwater roll and pitch instability occur. Posa and Balaras [12] reported the findings of computational research on the flow around a submarine model, focusing on how the appendages affected the propeller wake fields, using the high-fidelity LES approach. Morse and Mahesh [13] provided a novel analysis of turbulent boundary layers on streamlined bodies by examining the boundary layer generation at several points using LES. Rocca et al. [14] performed a numerical characterization of the hydrodynamic and hydroacoustic field of a fictitious underwater vehicle shape using large eddy simulation and a wall-layer model. Nevertheless, the LES method requires significantly more computational resources than the RANS method, a fact that limits its application to large-scale simulations. Thus, DES (detached eddy simulation) methods have recently emerged. Lungu [15,16] reported on a thorough investigation of the flow around a submarine model under straight-ahead and static drift conditions, using a range of turbulence models to assess the unique issues of large-scale flow separation involved. Wang et al. [17,18] discovered that the presence of the hull and the interaction with the free surface substantially impacted the propeller performance in a series of computational studies for underwater geometries operating close to the free surface. In order to compare the outcomes of URANS and DDES, Guo et al. [19] carried out numerical research for the flow around the submarine under the conditions of rudder deflection. The DDES (delayed detached eddy simulation) technique gave a greater capability for recording the flow field parameters around the submarine in constrained manoeuvring situations with noticeable flow separation. Regarding the approximation techniques, a study and comparison of different empirical methods conducted by Jones et al. [20], showed that, despite the fact that they can be used at an early design stage, in order to provide good results, careful calibration is needed.

Even though experimental methods are the most common way to predict the hydrodynamic coefficients, their costs still remain too high to be adopted given the huge captive matrix in 6-DoF, in particular for small vehicles (characterized by a low available budget), making them impossible to be carried out at an early stage of the design. Furthermore, during experimental tests, the influence of the support struts should be taken into consideration carefully. Although measurements of the hydrodynamic forces are conducted considering only the models, so not including the forces on the struts, their presence can significantly influence the flow around the submarine model. The challenges of such measurements extend beyond the supporting struts, encompassing various complexities. Boundary effects arising from interactions with tank walls and the bottom can impact the accuracy of measurements. Wave interference, generated within the towing tank, poses challenges in isolating the desired hydrodynamic responses. Additionally, viscous effects near the submarine surface and the accurate representation of the submarine model full-scale characteristics (new geometries, details like sonar domes and appendages) pose substantial challenges for researchers. Careful consideration and mitigation strategies for these difficulties are essential to ensure the reliability and relevance of the experimental results. Despite the above considerations, some experiments can be found in the literature. The most common models used in the literature are the DARPA SUBOFF and the Joubert/BB1/BB2 model. The SUBOFF model [21] is a typical of a nuclear-powered general-purpose attack submarine (SSN) configuration. Roddy [22] and Huang et al. [23] conducted experimental tests using the DARPA SUBOFF hull in order to investigate the stability and the control characteristics of several configurations with and without appendages. The Joubert submarine [24,25], designed for the Australian Department of Defense, is a conceptual model of a large diesel-electric submarine, specialized for anti-submarine duties (SSK), generally referred to in the literature as BB1. Further modifications to the aft control surfaces and sails [26] led to the BB2 configurations.

On the other hand, computational fluid dynamics methods make it possible to carry out the predictions without the presence of support struts. Furthermore, computations using CFD approaches can provide the contribution of the total force of each individual component of the submarine, for instance rudders, planes and sail, without additional complications of experimental measuring gauges. Some of the disadvantages of these techniques are the high computational costs when dealing with complex configurations, and the constant and rapid development of new numerical methods and simulation paradigms. Numerous investigations in the open literature have employed CFD simulations to rigorously examine surface ships, focusing on the extrapolation of hydrodynamic coefficients, contributing to a comprehensive understanding of the intricate fluid dynamics governing the behaviour of such vessels (see among others [27]), while as mentioned before, there is a difficulty in finding detailed investigations regarding the manoeuvrability of submarines. The aim of the current study is to explore the reliability of CFD predictions, through a systematic comparison with the available measurements, to feed the semi-empirical models of manoeuvrability of submarines usually adopted at the earlier stage of the design cycle as it is hard to find in the literature a full experimental campaign that has been simulated for different geometry configurations and different pitch and drift angles. Of great importance are also the simulations of the hydrodynamic forces acting on the control surfaces, when a rudder angle is present and when it is combined with different drift angles both in the horizontal and the vertical plane. Starting from the experience developed at the University of Genoa in the last few years (see, for instance, [28–30]), towing tank experiments of the

DARPA SUBOFF model are simulated using an open-source RANS solver to calculate the hydrodynamic forces and moments and the resultant coefficients.

In the following sections, after a short theoretical background presentation and the computational setup, the test case is presented, including the geometry of the model under investigation, and the tests performed (Section 2). In Section 3, the mesh sensitivity analysis is reported to assess the overall numerical uncertainty of the present procedure. The results are then presented in Sections 4 and 5, discussing the pure drift test and the rudder test outcomes, respectively. Finally, a summary of the conclusions of the current study is reported.

2. Computational Setup and Test Case

In the current study, numerical simulations are performed with the open-source CFD library OpenFOAM [31]. OpenFOAM provides users with full access to the source code, allowing them to customize and modify the software to suit their specific needs. This flexibility is not typically available in commercial software, which may limit the user's ability to customise it. The governing equations are discretised using the finite volume method with the second-order upwind scheme. For the pressure–velocity coupling, a guess-and-correct procedure, the SIMPLEC (semi-implicit method for the pressure-linked equations) algorithm is employed. The selection of the SIMPLEC algorithm is based on its good convergence rate, especially for steady state analyses, so fewer iterations and a reduced computational time [32] is needed. The incompressible steady RANS system of equations (see Equation (1)) is used to model the flow around the UV geometry.

$$\begin{cases} \dfrac{\partial u_i}{\partial x_i} = 0 \\ \rho u_j \dfrac{\partial u_i}{\partial x_j} = -\dfrac{\partial p}{\partial x_i} + \dfrac{\partial}{\partial x_j}\left(\mu \dfrac{\partial u_i}{\partial x_j} - \rho \overline{u'_i u'_j}\right) \end{cases} \tag{1}$$

where F_i is the body forces, p is the time averaged pressure, μ and ρ are the molecular viscosity and density of the fluid, respectively; u_i and u'_i are the time averaged velocity components and the fluctuating velocity components, respectively, both in Cartesian coordinates x_i $(i = 1,2,3)$ and $-\rho\overline{u'_i u'_j}$ is the Reynolds stress tensor.

For the purpose of estimating the Reynolds stress tensor $-\rho\overline{u'_i u'_j}$, hence, to mathematically close the problem, several turbulence models can be adopted. In the present case,four different models are used, $k-\omega$ [33], shear stress transport $k-\omega$ [34], $k-\epsilon$ [35,36] and realizable $k-\epsilon$ [37]. Regarding the schemes, Table 1 shows the selected methods.

Table 1. Schemes used in the current simulations.

Terms	Scheme
Convective term	Bounded Gauss LinearUpWindV (U) Bounded Gauss upwind (k, ω, R, ϵ)
Diffusive term	Bounded Gauss upwind (k, ω, R, ϵ)
Time integration	SteadyState
Laplacian term	Gauss linear limited 0.3

In the present simulations, two linear solvers are used to solve the equations. For the pressure equation, the GAMG (generalized geometric-algebraic multigrid) solver with Gauss–Seidel smoothing was used to ensure robustness and efficiency. For the other equations (such as the momentum or the turbulent ones) the smoothSolver with Gauss–Seidel smoothing is utilized. This solver is a common choice in OpenFOAM simulations and was chosen for its efficiency and robustness.

In the simulations of pure drift and rudder tests, a prismatic box was selected as the computational domain around the UV model, with the upstream boundary located at $2L$ ahead of the fore part of the UV (where L is the length of the submarine), the downstream boundary at $3L$ from the aft tip, and lateral sides as well as the top/bottom boundaries at $1.5L$ from the cylindrical body (Figure 1). Figure 1 also shows the computational domain with the assigned boundary conditions. On the right side of the computational domain, a velocity inlet is assigned (in blue in figure), while on the left side the pressure outlet (in red) is forced. The other surfaces are considered as symmetry planes while on the submarine surfaces, a no-slip wall condition is assigned. The sizes of the domain were such that the far field flow can be considered undisturbed, so avoiding the situation that the boundary conditions affect the flowfield in proximity of the submarine.

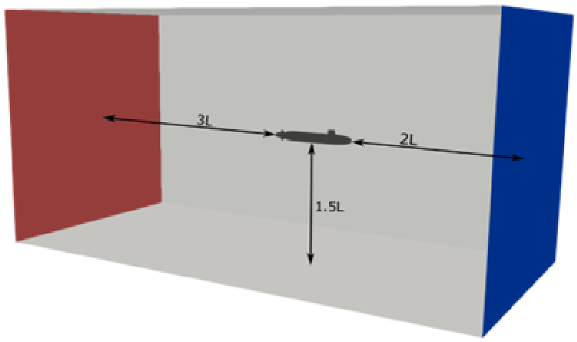

Figure 1. Main dimensions of the computational domain.

The mesh was generated by the open-source tool CfMesh v1.14 [38], which generates a hex-dominant Cartesian mesh around the geometry of interest. Proper mesh-refinement regions, inversely proportional to the distance from the submarine, were introduced to better capture the flow field in the UV near field, with approximately $3M$ cells for the barehull and $3.7M$ cells for the fully appended configuration. A sketch of the obtained mesh for zero drift angle is depicted in Figures 2 and 3, showing the boundary layer and the mesh refinement close to the body more closely.

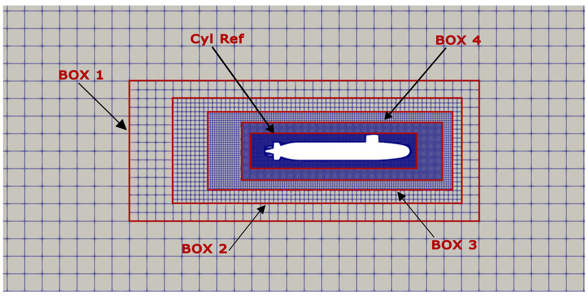

Figure 2. Box and cylindrical refinements of the domain.

Additional local refinements were used to better describe the rudders or sternplanes, in particular when a deflection angle is present, in order to adequately simulate the gap between the appendages and the axisymmetrical hull surface (Figure 4).

As for the simulations having angular velocities q and r, a new, circularly shaped domain was adopted. Figure 5 shows the boundary conditions assigned to the circular domain, with the the velocity inlet in blue and the pressure outlet in red. As in the case of pure drift tests, the other far field surfaces are handled as symmetry planes. The boundary condition on the surfaces of the submarine is a no-slip wall boundary condition. A section of the computational domain used for the pure rotation tests with its refinements is also illustrated. Both these setups follow the mesh layout already successfully adopted for surface vehicles in [29], having the overall domain modelled by the blockMesh OpenFOAM command, while the smallest block is modelled separately by the usage of the

CfMesh library. This is because CfMesh affords the capability to generate a high-quality mesh, ensuring the attainment of precision and accuracy, even in the presence of complex geometric configurations.

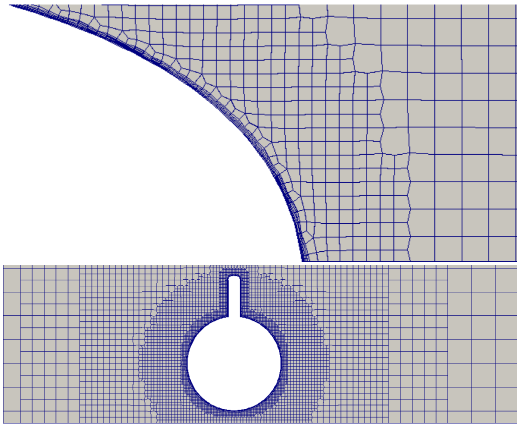

Figure 3. Detail of the mesh refinement close to the body.

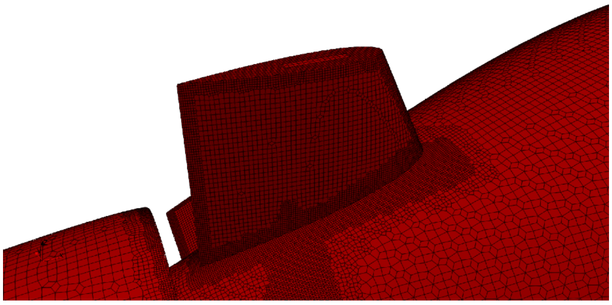

Figure 4. Local refinement for the stern appendages.

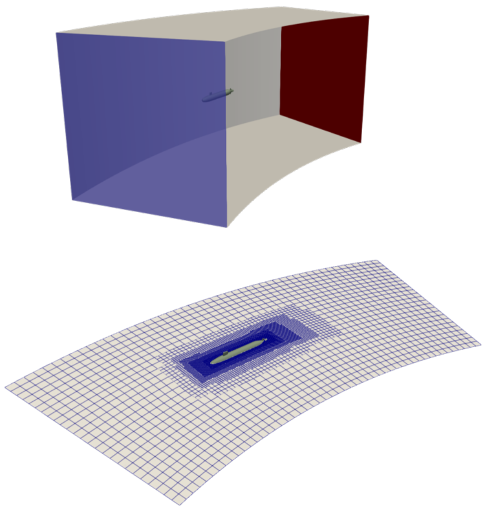

Figure 5. Local refinement (cylindrical) for the stern appendages.

In order to better analyse the turbulent viscous flow around the walls and thus deal with the near wall region in affordable computational times, the wall functions, also implemented in OpenFOAM, were used. These functions are based on empirical equations used to bridge the inner region between the wall and the fully developed turbulence region. In order to ensure the validity of these functions, the first cell centre needs to be within the log-law region from the walls. In the author's previous work [39], simulations with both y^+ between 30 and 50, as well as, $y^+ < 1$ were run, showing that the results are not significantly affected by the y^+ selection. This is also confirmed by other authors, such as in [40] where a sensitivity analysis of y^+ for different turbulence models is presented. The findings of this study suggest that, for turbulence models such as kOmega and kEpsilon, the values of longitudinal and lateral force exhibit a high degree of insensitivity to y^+, whereas this is not true for more sophisticated turbulence models, such as the baseline Reynolds stress model (BSLRSM), which show a higher sensitivity to the values of y^+. Thus, considering the above findings and also considering the computational effort connected to a smaller y^+, a higher y^+ was preferred. In the simulations, a mean value of y^+ between 30 and 150, the limits of the wall functions, was guaranteed (similar to [41]). Therefore, a value of $y^+ = 50$ was fixed, as a starting point. Table 2 shows the obtained average values of y^+ for the different components of the fully appended configuration.

Table 2. The requested and the obtained average values of y^+.

Component	Requested y^+	Obtained y^+
Hull	50	38.42
Ring Wing	50	48.37
Sail	50	48.37
Upper Rudder	50	44.74
Lower Rudder	50	44.74
STB Sternplane	50	44.74
PS Sternplane	50	44.74

In Figure 6, the obtained values of the y^+ are shown over the surface of DARPA SUBOFF. It is evident that the values fall within the range of the applicability of the wall function as requested by the models. The y^+ pattern highlighted in the figure is a consequence of the adopted grid generator, but in analysing the resulting smooth wall shear stress distribution over the submarine surfaces (Figure 7), it is clear that the proposed mesh layout can be considered adequate for the present analyses.

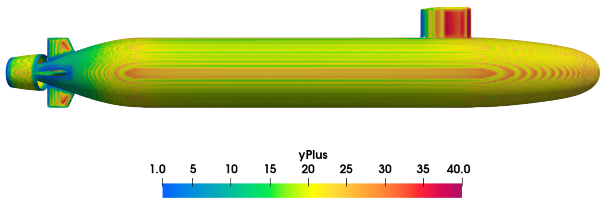

Figure 6. The y^+ values for ther fully appended configuration.

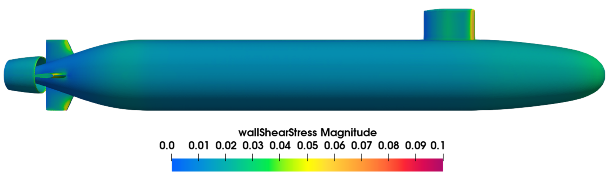

Figure 7. The wall shear stress [m^2/s^2] values obtained for the fully appended configuration.

The UV under investigation is the SUBOFF model, designed and tested in the David Taylor Research Centre (DTRC) for the Defense Advanced Research Projects Agency (DARPA). This model was selected as it is the only submarine for which a significant amount of data were available in the open literature. This because the DARPA SUBOFF model was developed as part of a research programme, which involved a significant amount of experimental testing and validation of the model. Data from the DARPA SUB-OFF program, i.e., an extensive campaign of captive model tests, are publicly available and are widely used to validate and improve CFD models for submerged bodies. The model provided by DTRC is an axisymmetric body, having a sail, four symmetric stern appendages in a cross configuration, and therefore, two horizontal stern planes and two vertical rudders (in the DTRC report, three different configurations related to the trailing edge position of the appendages are shown), and two configurations of ring wing (number 1 and number 2) supported by small struts in an "X" configuration. All the simulations present in this study consider the scale model, as in the experiments, at a model speed of 3.34 m/s, which corresponds to a Reynolds number (based on the length between perpendiculars) of about 14 million. According to DTRC experiments, the hydrodynamic force and moment coefficients show slight variations, becoming almost constant for values of Reynolds number above 14 million, meaning that the scale effects between model and full scale would be negligible for the purpose of making stability and control predictions. The main dimensions of the model and its reference system are given in Figure 8, whereas the equations used to design the geometry of the model can be found in the reference literature [21]. The adopted reference frame is centred about amidship along the symmetry axis of the hull (located at $x = 2.013$ m with respect to the aft perpendicular, see Figure 8, which corresponds to the mid distance between the two perpendiculars). The x-axis is positive, pointing towards the fore part of the submarine, the y-axis is pointing towards the starboard side, and the z-axis is pointing downwards. Angles β and α indicate the drift angle in the horizontal and the angle of attack in the vertical plane, respectively, whereas r and q are the angular velocities in the two planes. The submarine rotation, in the horizontal plane is positive for β towards the starboard side and α going upwards in the vertical plane. The measurements, as well as the outcomes of the numerical simulations, of the rudders and the sternplanes of the submarine are evaluated with respect to local reference systems. Angles δ_S and δ_R represent the sternplane (for vertical motions) and the rudder (for horizontal motions) angles, respectively.

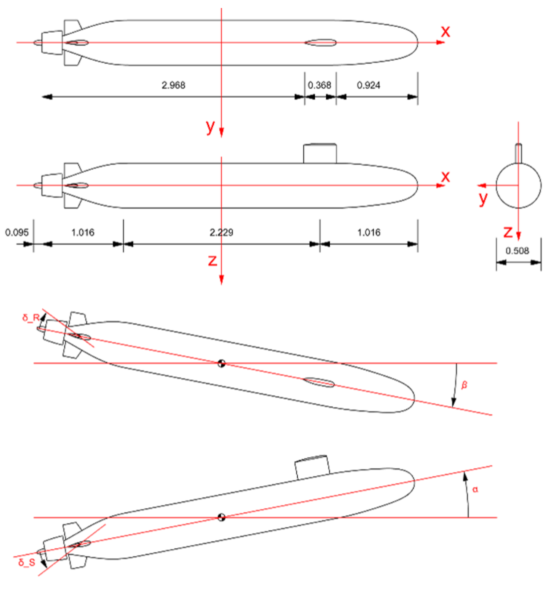

Figure 8. Main dimensions in meters of the DARPA SUB-OFF and reference system.

The forces collected and analysed in this study are the longitudinal force X, the lateral force Y and the vertical one Z, while the moments are K about the x-axis, M about the y-axis and N about the z-axis. The forces and moments are made non-dimensional as follows:

$$\begin{array}{lll} X' = \frac{X}{\frac{1}{2}\rho L^2 V^2} & Y' = \frac{Y}{\frac{1}{2}\rho L^2 V^2} & Z' = \frac{Z}{\frac{1}{2}\rho L^2 V^2} \\ K' = \frac{K}{\frac{1}{2}\rho L^3 V^2} & M' = \frac{M}{\frac{1}{2}\rho L^3 V^2} & N' = \frac{N}{\frac{1}{2}\rho L^3 V^2} \end{array} \quad (2)$$

where L is the distance between the perpendiculars (used also by DTRC) and V is the model scale velocity of experiments, equal to 3.34 m/s.

The tip of the submarine stern was truncated, considering a total hull length of 4.26 m, equal to the length between perpendiculars. The truncated part is 2.2% of the overall length of the UV. This simplification is also made to reduce the computational cost of the model; the tip is much smaller compared to the rest of the body, and a finer mesh would have been required in that region to represent the exact geometry. The truncation of the SUBOFF has been already used also in other studies [42–44] for the mounting of the sting support. For these reasons, the proposed simplification should affect in a negligible way the expected forces. Figure 9 shows the 3D model of the submarine with the truncated tip in the stern region used for the present CFD calculations.

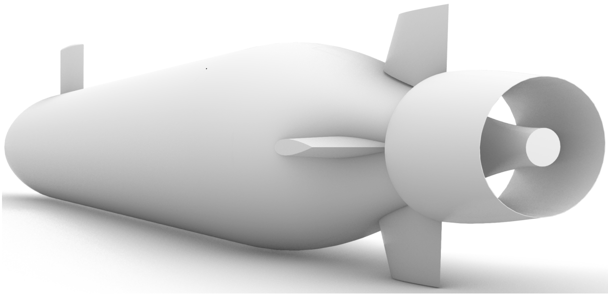

Figure 9. The truncated stern tip of the submarine.

Regarding the stern appendages (stern rudders, planes, and ring wing), as mentioned before, in the captive model experiments carried out by the DTRC institute, three different configurations were considered. Each one differs from the others by the axial position of both the rudders and "ring wing", as the nozzle surrounding the stern of the hull is called in the report of DTRC. In the current paper, the "baseline stern appendage location", using the ring wing number 1 with the trailing edge of the rudder at $x = 4.007$ m, is modelled. To further simplify the adopted geometry, the supportive struts of the wing have been neglected, as shown in Figure 10.

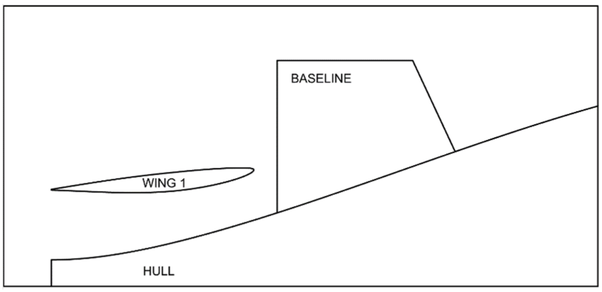

Figure 10. Section of the submarine and the used configuration of the ring wing (number 1).

To provide a sufficient gap for stern appendage movement, a slight offset of the appendages from the axisymmetric hull surface is introduced. It is quite interesting to take into consideration the possible effect that this gap might have on the stern appendages' performance. Since the correct layout of these appendages is not clear from the paper of Groves et al. [21], two different approaches (Figure 11) can be used for this offset: one by cutting with a straight line the root of the appendage, the other by shifting the appendage (then maintaining its initial span).

In Figure 12, the comparison between calculations of the two different configurations and the values measured from DTRC on the upper rudder are reported for the non-dimensional longitudinal and lateral force, respectively X' and Y'. As expected, the shifted version provides a higher force because it has a slightly bigger area (about 5%). Comparing the measurements with the obtained CFD results for the two configurations, the truncated one gave more reliable results, and so it is used in the current study.

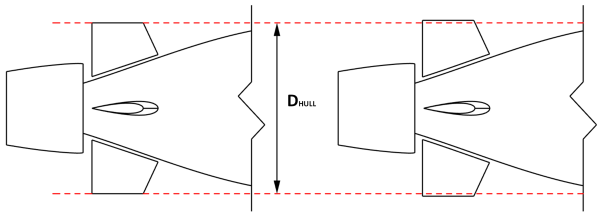

Figure 11. The two different possible solutions for the stern appendages' motion; on the right, the truncated, and on the left, the shifted solution; red dashed line shows the hull diameter.

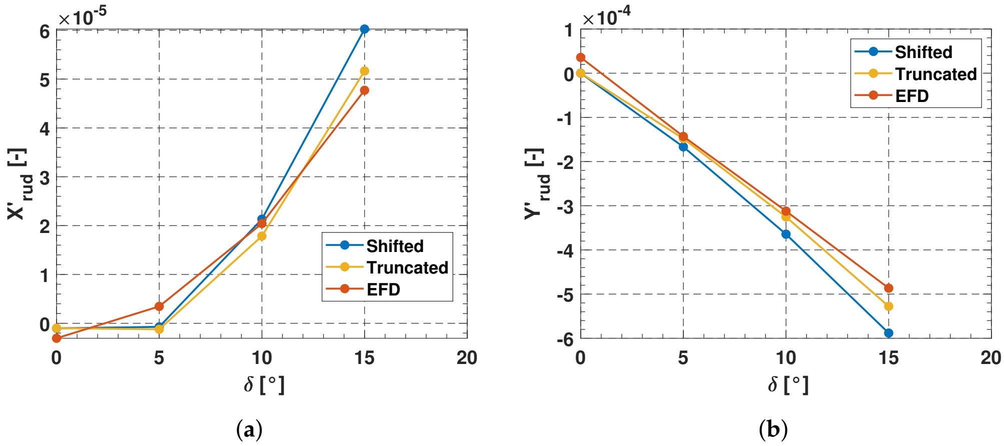

Figure 12. Comparison between the two configurations of the stern appendages (shifted and truncated); fully appended, 0° drift; (**a**) longitudinal force; (**b**) lateral force.

A campaign of captive model experiments performed in the David Taylor Model Basin was conducted for both vertical and horizontal planes of motion at deep submergence. Captive model experiments were performed for different configurations of the submarine, never including the presence of the propeller. The investigated drift angles in the horizontal and vertical plane, as well as the rudder and sternplane angles are summarized in Table 3. Given the symmetry of the submarine, only the positive angles are used for the horizontal motions. In the vertical plane, both positive and negative angles are accounted for due to the asymmetry induced by the presence of the sail.

Table 3. Campaign of the captive model tests performed by DTRC, where *BH* is the barehull configuration; *BHS*, barehull with the sail; *BHSTAP*, barehull with stern appendages; *BHRIW*, barehull with ring wing 1 and *FA* the fully appended configuration.

Condition	Configuration	β [°]	α [°]	δ_R or δ_S [°]
Pure drift (Horizontal)	*BH/BHS/BHSTAP /BHRIW/FA*	0/+18	0	0
Pure drift (Vertical)	*FA*	0	−18/+18	0
Rudder Tests	*FA*	0	0	+5/+15
Combined Tests (Horizontal plane)	*FA*	0/+18	0	+5/+15
Combined Tests (Vertical plane)	*FA*	0	−18/+18	+5/+15

3. Numerical Model

To assess the reliability of a computational fluid dynamics analysis, two activities are essential: verification and validation. The former concerns the order of convergence with respect to the grid density and the associated numerical uncertainty, the latter the suitability of the mathematical model as a description of the physical problem. This section is divided into two parts: the first part presents the verification process realised using the kOmega SST turbulence model, and the the second half provides an analysis of the results obtained with different turbulence models.

3.1. Mesh Sensitivity Analysis

Regarding the verification, following Richardson's extrapolation and starting from the reference grid size (*gridII*), two additional grid sizes are defined, one coarser (*gridI*) and one finer (*gridIII*), having about $2M$ cells (*I*), $3M$ (*II*) cells and $7M$ cells (*III*). In Figure 13, the three different mesh grids are shown, and in Figure 14, detail of the refinement region closer to the hull is illustrated. All the meshes share the same arrangement of the refinements.

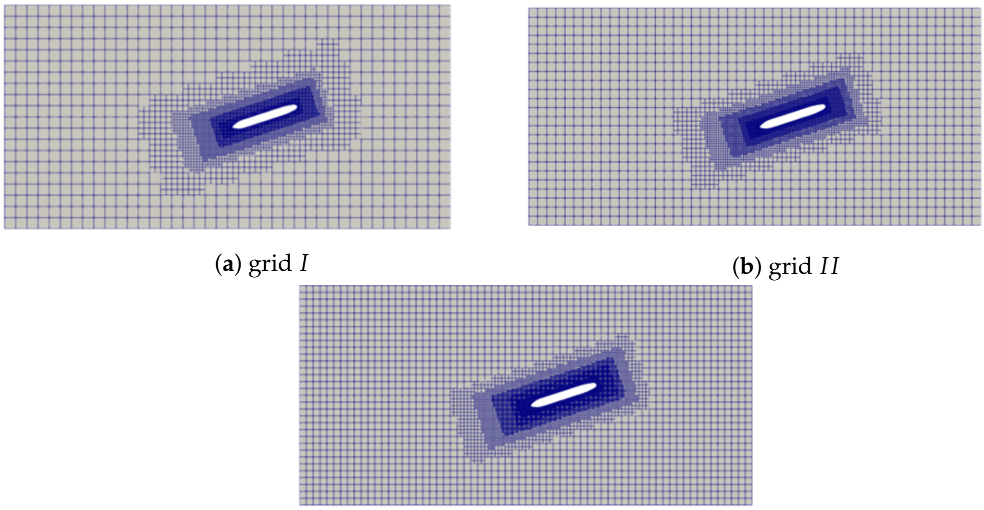

(**a**) grid I (**b**) grid II (**c**) grid III

Figure 13. The three different mesh grids; (**a**) coarse; (**b**) base; (**c**) fine for 18° drift angle.

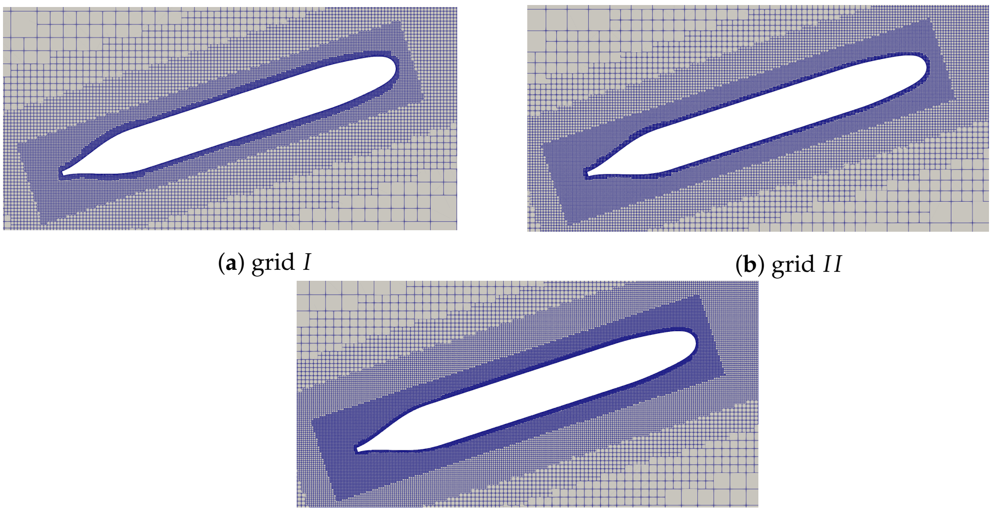

(**a**) grid I (**b**) grid II (**c**) grid III

Figure 14. Detail of the refinement around the hull for the three different mesh grids; (**a**) coarse; (**b**) base; (**c**) fine for 18° drift angle.

The mesh refinement is achieved varying all the dimensions of the cells in order to obtain equally distributed smaller cells. The input sizes of the cells are such that the grid refinement factor $r = \frac{h_{coarse}}{h_{fine}}$ is greater than 1.3, as prescribed by the extrapolation procedure [45,46]. For this mesh analysis, three global quantities are considered (in non-dimensional form): axial force (X'), lateral force (Y') and moment about the z-axis (N'). To enlarge the analysis, all the different geometry configurations were explored for all the different angles present in the DTRC report. In Figures 15–17, comparisons between the three different grids, for the nondimensional quantities X', Y' and N' in the three different configurations BH, $BHSTAP$ and FA are collected.

Data showing the lateral forces and the yaw moments are almost insensitive to the mesh when using the coarser one where, in principle, higher discrepancies could be expected. The longitudinal component of force, differently, shows a slightly higher sensitivity to the mesh size. The numerical uncertainty originating from the spatial discretization is analysed and estimated according to the Richardson extrapolation, using the grid convergence index (GCI) as a parameters. This index is suggested by Roache to provide a consistent way to describe the findings of grid convergence studies. For the verification analysis, as the grid changes, the solution should not change much and should approach an asymptotic value. CGI is a measure of the percentage the computed value is away from the value of the asymptotic numerical value. Small values of CGI indicate that the computation is within the asymptotic range. The convergence index is calculated as follows:

$$GCI^21 = \frac{1.25e_a^{21}}{r_{21}^p - 1}, \tag{3}$$

where the e_a^{21}, indicates the approximate relative error between the obtained values of a variable ϕ, important for the purpose of the simulation study:

$$p = \frac{1}{\ln r_{21}} \left| \ln \left| \frac{\epsilon_{32}}{\epsilon_{21}} \right| + q(p) \right| \tag{4}$$

$$q(p) = \ln \left(\frac{r_{21}^p - s}{r_{32}^p - s} \right) \tag{5}$$

$$s = 1 \cdot sgn \left(\frac{\epsilon_{32}}{\epsilon_{21}} \right) \tag{6}$$

where $\epsilon_{32} = \phi_3 - \phi_2$ and $\epsilon_{21} = \phi_2 - \phi_1$. Subscripts 1, 2 and 3 are associated to the three different grid densities used for this study, respectively $gridI$ (1), $gridII$ (2) and $gridIII$ (3). Equation (5) can be solved using fixed-point iteration, with the initial guess equal to the first term $(q(p) = 0)$. Tables 4 and 5 show the different values of GCI for the Y force and the N moment for the BH, $BHSTAP$ and FA configurations. These values of the grid convergence index, considered as an average of the values calculated for each angle included in the analyses, confirm the very good rate of convergence observed in the figures and permit the use of the base mesh ($gridII$) for all the subsequent analyses since results can be considered reasonably independent from the adopted mesh.

Table 4. Mean values of GCI of Y force, for 3 different configurations.

Configurations	**GCI**
BH	0.40%
BHSTAP	1.64%
FA	3.21%

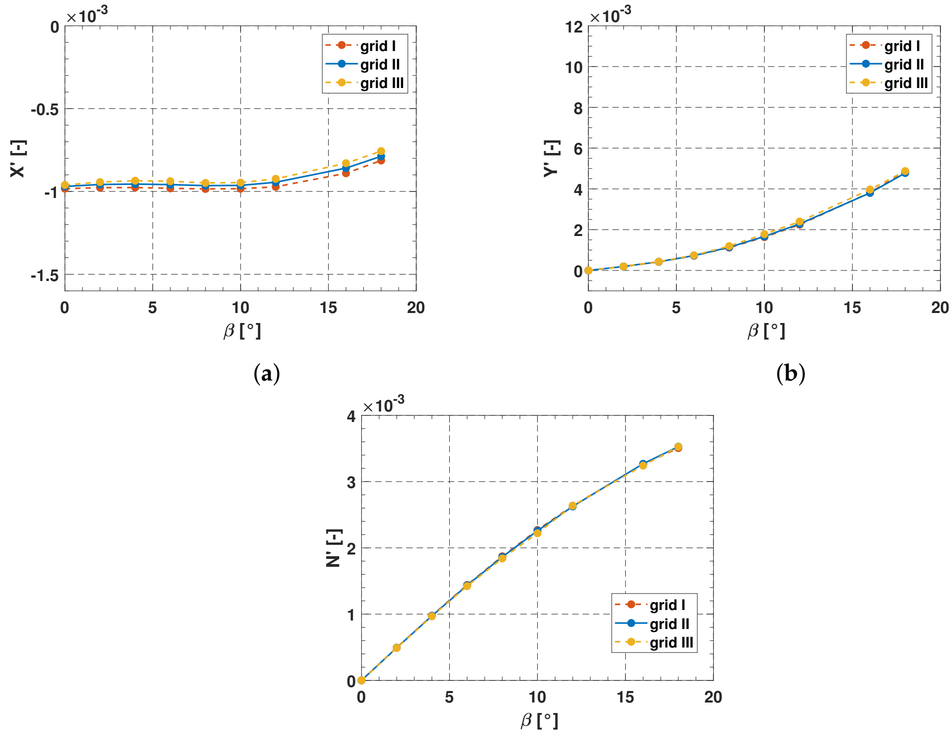

(**a**) (**b**)

(**c**)

Figure 15. Values of X' (**a**), Y' (**b**) and N' (**c**) for the three different mesh grids, barehull configuration.

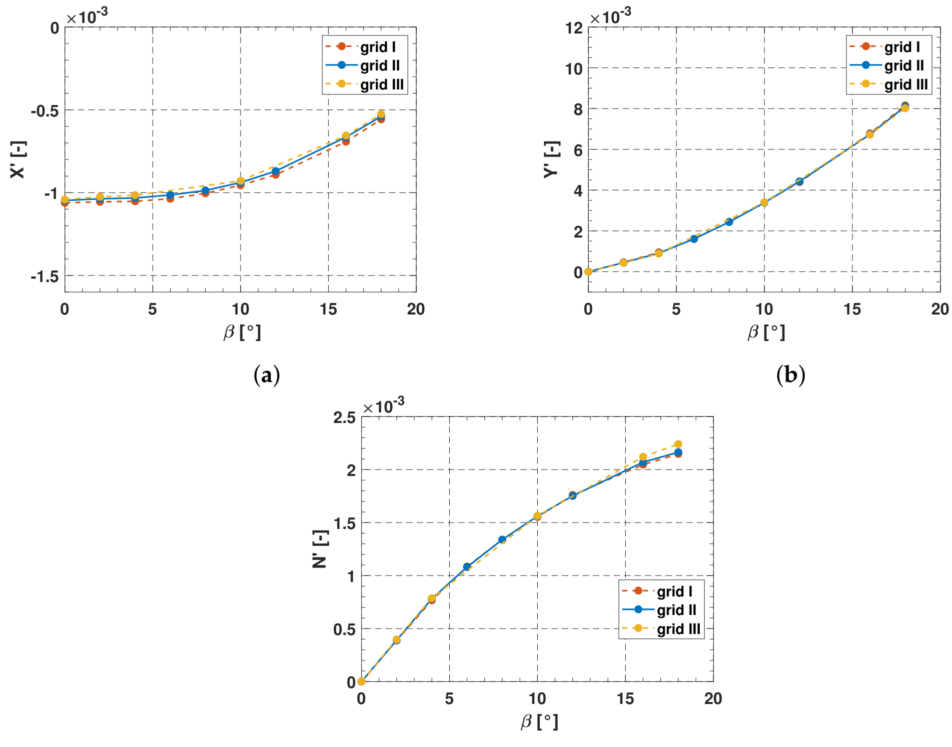

(**a**) (**b**)

(**c**)

Figure 16. Values of X' (**a**), Y' (**b**) and N' (**c**) for the three different mesh grids, barehull with stern appendages configuration.

Table 5. Mean values of GCI of N moment, for 3 different configurations.

Configurations	GCI
BH	0.45%
BHSTAP	1.82%
FA	2.78%

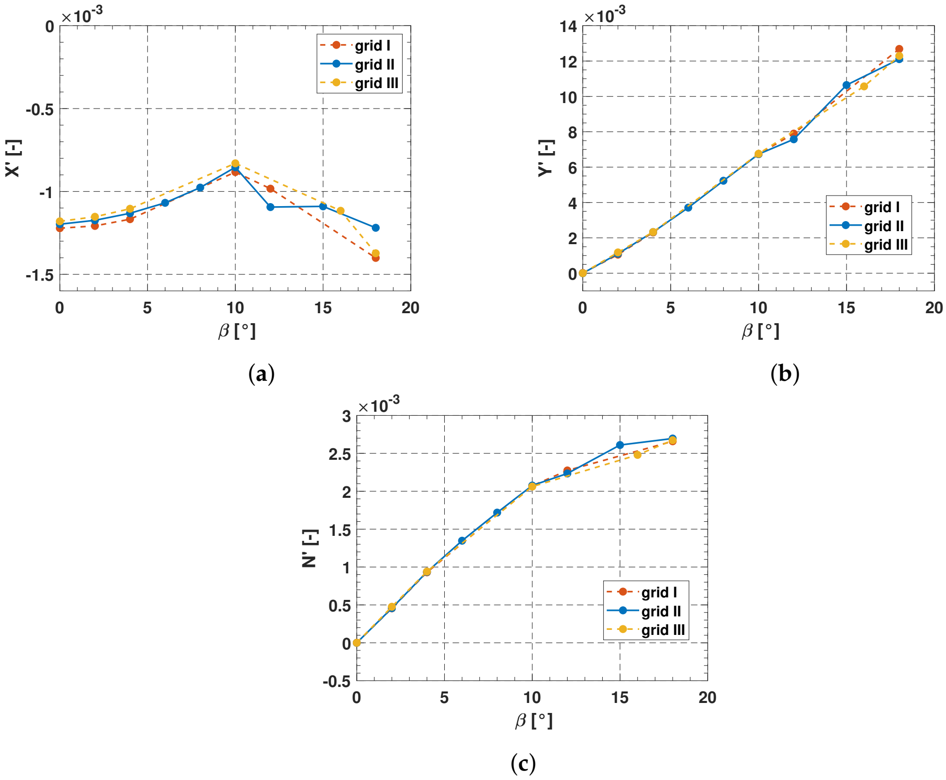

Figure 17. Values of X' (**a**), Y' (**b**) and N' (**c**) for the three different mesh grids, fully appended configuration.

3.2. Turbulence Model Analysis

In the preceding subsection, the effect of grid refinement on simulation accuracy was analysed. In this stage of the study, four different turbulence models present in OpenFOAM are examined, kOmega, kOmega SST, kEpsilon and realizable kEpsilon for the barehull configuration. Several turbulence models are known to forecast certain types of flows, such as boundary layers, shear layers, wake flows or rotating flows, better than others. It is apparent that, currently, there is no universally applicable turbulence model that can consistently and accurately predict all turbulent flow scenarios. As a result, it becomes imperative to validate the suitability of the chosen turbulence model for the particular flow being analysed. Table 6 shows the comparison between the different turbulence models and the data from the DTRC. The two kOmega models give similar results, as well as the two kEpsilon between them, with the kOmega models showing an estimated mean error of 19% and 7% for the lateral force and the yaw moment, whereas the kEpsilon show 10% and 2%, respectively. Thus, in the next sections, all results are obtained with kEpsilon-based models.

A possible explanation for the differences between the turbulence models and the experimental data may be found in the cross-flow separation. In Figure 18, it is evident how the surface pressure distribution and the cross-flow in the boundary layer varies by increasing the drift angle. In fact, in Figure 19, it can be noted how this phenomenon generates two symmetrical streamwise vortices, originating from the downstream side of the body. As the drift angle increases, these vortices become more prominent and extensive.

In general, previous numerical investigations of the flow around a prolate spheroid, similar to the geometry of the current submarine's hull, have observed similar effects [47–50].

Table 6. Comparison between the DTRC data and the predicted values of the lateral force Y' and the yaw moment N' for the different turbulence models; barehull configuration; three different drift angles $\beta = 4°, 6°, 18°$.

	$Y' \cdot 10^{-4}$			$N' \cdot 10^{-4}$		
	4°	**6°**	**18°**	**4°**	**6°**	**18°**
DTRC	4.49	8.86	73.55	9.96	13.85	29.86
kOmega	4.55	7.94	53.64	9.57	14.03	34.77
kOmegaSST	4.27	7.29	47.79	9.73	14.34	35.27
kEpsilon	4.63	8.00	59.66	9.52	13.97	33.46
realizable kEpsilon	3.97	8.77	61.39	9.66	13.70	32.64

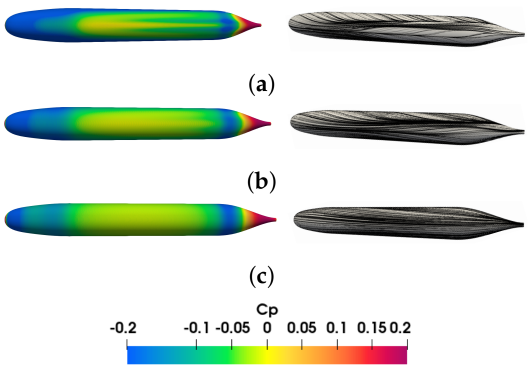

Figure 18. Surface pressure contours and limiting-wall streamlines on the bare hull for three different drift angles $\beta = 18°$ (**a**), $10°$ (**b**) and $4°$ (**c**).

The vortices are illustrated in Figure 19 using an iso-surface of the second invariant of velocity, found in the literature as "Q-criterion" [51]. From the physical point of view, the flow around the barehull configuration after a transient phase starts separating in two counter rotating vortices on the downstream side of the hull. This phenomenon is well captured by the CFD predictions. Nonetheless, small errors in the estimation of the starting point of the flow separation might lead to important errors in the description of the pressure, in the velocity fields around the body, especially in large drift angle configuration, where these phenomena become more prominent.

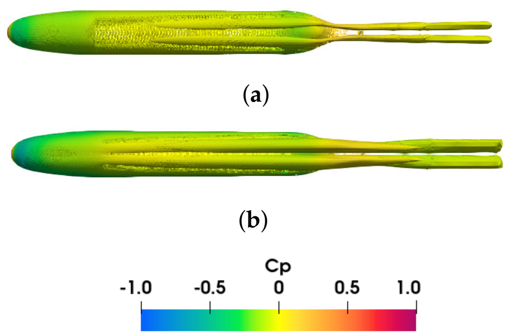

Figure 19. Iso-surface of Q coloured by pressure coefficient magnitude for the barehull configuration, for two different drift angles $10°$ (**a**) and $18°$ (**b**).

A closer look at the vortices region shows the same results as Kotapati et al. [48] and Subrahmanya et al. [49] (Figure 20). For small drift angles, Figure 20a shows the vortices are close to the hull, having a flat elliptic shape. As the drift angle increases and moves closer to the stern, the vortex starts detaching from the body, increasing in size and becoming more circular (Figure 20c).

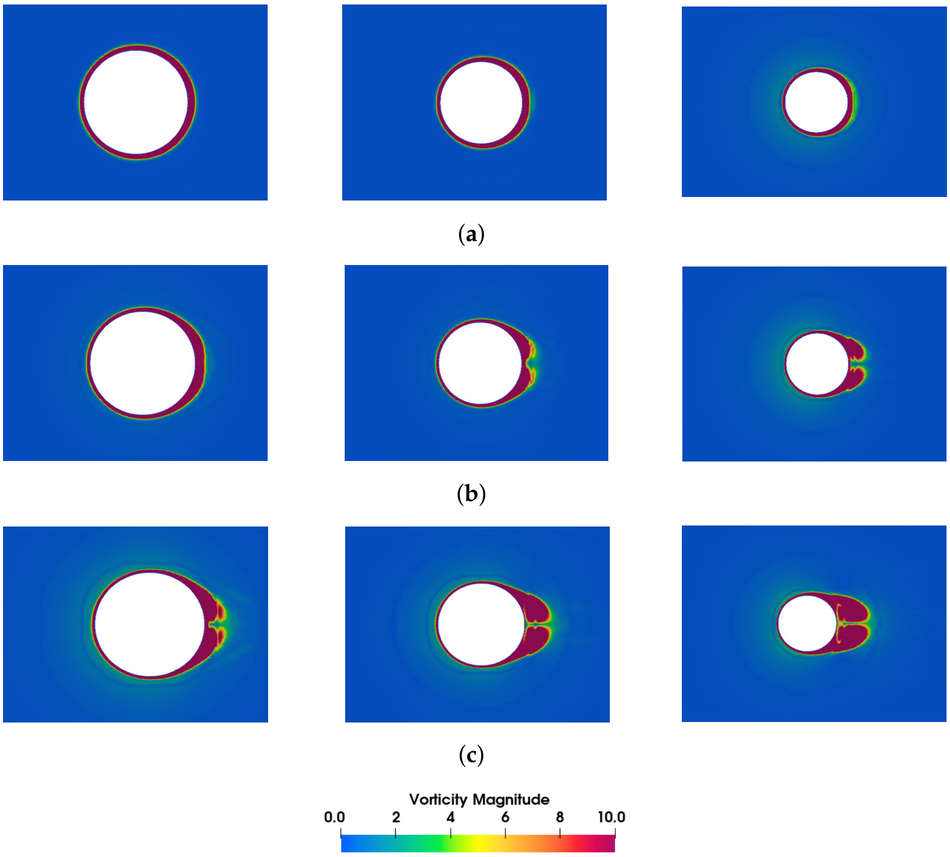

Figure 20. Vorticity around the axisymmetic hull for drift angle values of 4° (**a**), 10° (**b**) and 18° (**c**), sections at 0.55L, 0.35L and 0.15L.

Figure 21 shows the vorticity around the axisymmetric hull modelled with four different turbulence models, kOmegaSST, kOmega, kEpsilon and realizablekEpsilon. It is clear how similarly the two initial turbulence models represent the shaded vortices. However, there are some minor variations, such as the vorticity magnitude in the core of the vortex, which causes the yellow and red scale zones to enlarge slightly. The vortices grow bigger and farther out from the body and from one another. In contrast, the kEpsilon models seem more complex and detailed, with more irregularities and small-scale features, whilst the kOmega models seem smoother and simpler.

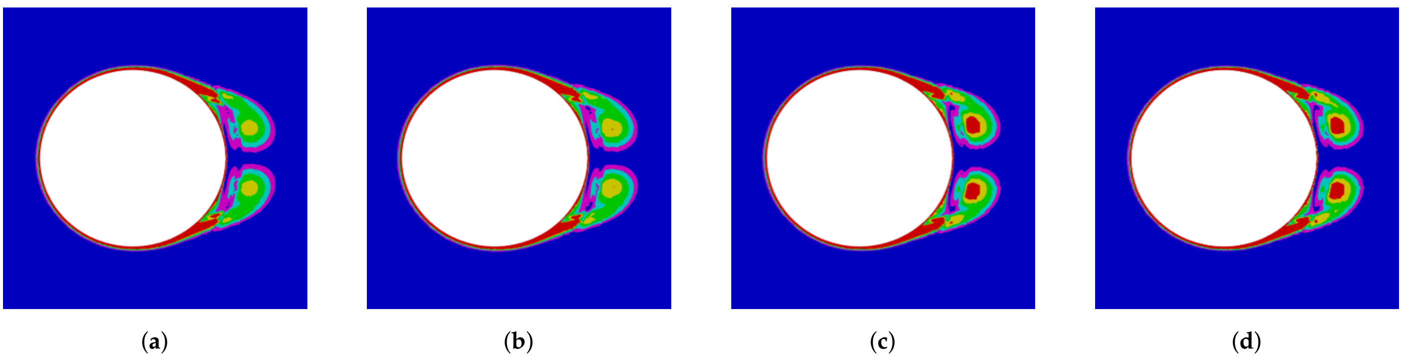

Figure 21. Vorticity around the axisymmetric hull modelled with kOmegaSST and kOmega (**a**,**b**); kEpsilon and realizablekEpsilon (**c**,**d**) for 18° drift angle.

The prominent part of this investigation lays in the impact that these models have on the sectional forces. The submarine was divided into 100 transversal sections, and the forces acting in each section were measured. Figure 22 shows the sectional lateral force coefficient C_y for the different turbulence models.

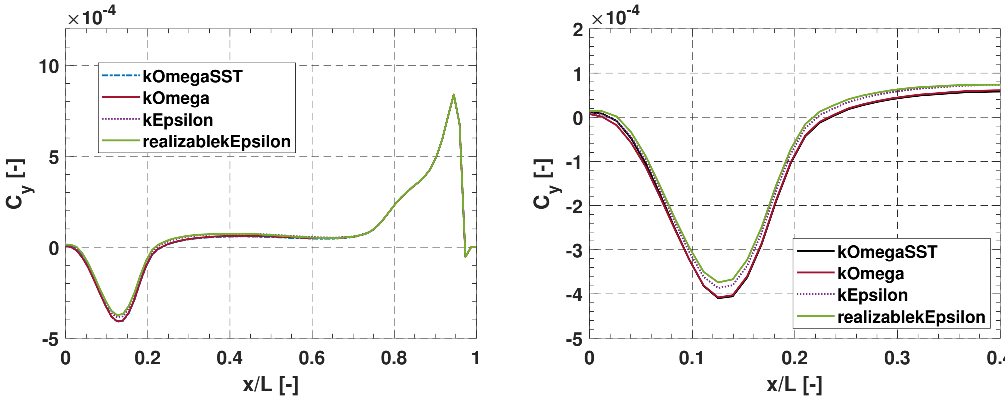

(**a**) (**b**)

Figure 22. Comparison between the sectional forces of the simulations with the different turbulece models for 18° drift angle (**a**); (**b**) A closer look at the region where the main differences are present.

Observing the values in Table 6 and the trends in Figure 22, it is evident how the closer the outcomes are to the experimental data, the less the negative force in the stern region. This observation validates the initial hypothesis of the authors, that the magnitude of the force at the stern is overestimated by the initial simulations. These findings may also provide insight into how slight alterations in the pressure field may have a substantial impact on the intensity and location of the subsequent forces. This is primarily, because, during the manoeuvre, the difference between the positive bow force and the negative stern component causes the later force. As a result, a tiny disparity that is localised on the pressure field has a significant impact on the forces as a whole. In a previous study [39], the pressure and wall shear stress distribution around the underwater vehicle were also illustrated, giving a hint about the small influence that the wall shear stress might have on the lateral forces.

4. Results: Pure Drift Tests

In the present section, the results of the CFD simulations are collected and compared with the available experimental measurements. In the current study, the measurements conducted by DTRC are exploited for benchmarking purposes. For the validation of the CFD predictions, all the pure drift and rotation conditions are taken into consideration in both the horizontal and vertical planes, inclusively of the pure rudder and sternplane angles tests, as well as the combined tests. The analyses have been carried out for all the configurations tested in the towing tank to deliver an assessment as wide as possible of the accuracy of CFD calculations in the prediction of hull, appendages and ring wing contributions to UV forces and moments.

4.1. Barehull Configuration

Figure 23 shows the comparison between the numerical simulations of the current study and measurements from the experiments of the DTRC. The outcomes of the experimental tests are in orange; a blue line identifies the numerical calculations while a dashed red line represents the linear part of the experimental data as specified in the DTRC report. Numerical results show that the trends between the experimental and the computed data are in good agreement, especially the linear part of the lateral forces and yaw moment.

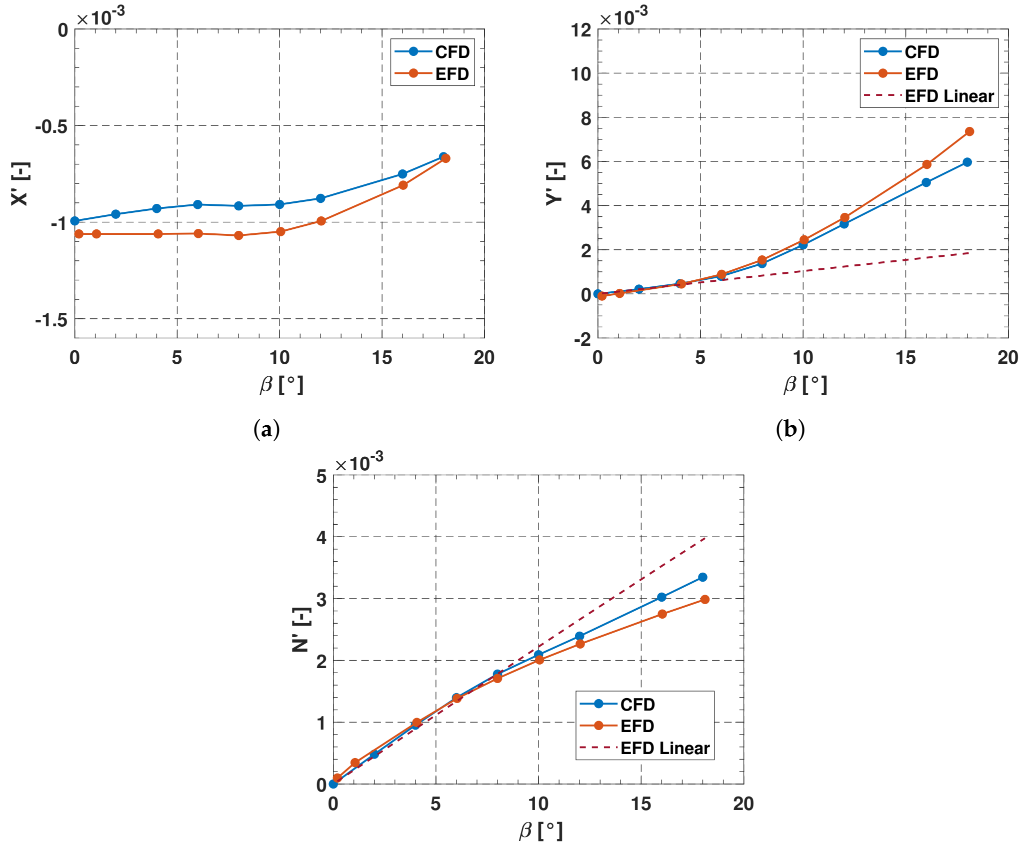

Figure 23. Comparison between the numerical results (blue) and experimental data (orange) of X' (**a**), Y' (**b**) and N' (**c**) for the barehull configuration. The linear component is shown in dashed red line.

For drift angles higher than 6°, nonlinear phenomena become more notable, leading to a gap between the measured and the predicted curves. Similar to the results obtained by Subrahmanya et al. [49], the force Y' is underestimated compared to the experimental data (Figure 23b), whereas the moment is slightly overpredicted (Figure 23c), even though the trend in both cases is well predicted. To sum up, the quality of simulation results is very good in terms of linear derivatives, but with not negligible differences in the nonlinear range. Nevertheless, as it will be stated in the next sections, this mismatch becomes minor when considering the hull with appendage configurations that are close to real shapes, so in line with the design perspective.

4.2. Barehull with Ring Wing

Figure 24 compares measurements and calculations in the case of the barehull with the ring wing. Qualitatively, the CFD calculations follow the physics of the phenomenon. The presence of the ring wing leads to an increment of the lateral forces compared to that of the barehull alone (see Figure 25). For both experimental data and CFD predictions, there is an increment of about 10% of the maximum value of the lateral force between the BH configuration and the BHRIW [52,53]. The CFD results slightly overpredict the effect of the ring. This can be mainly ascribed to the fact that its presence has an impact on the region that was affected by the previously noted differences in the lateral forces. As in the previous case, the linear part is well captured by the simulations, while some differences in the nonlinear part still remain observable.

4.3. Barehull with Stern Appendages

In Figure 26, the forces and moments predicted for the configuration with stern appendages are illustrated. It is clear how the CFD calculations, as far as the lateral forces are concerned, show a better agreement with measurements for drift angles up to 10°. Also, the results of the yaw moment for this configuration are better if compared to those obtained for barehull or barehull plus ring wing configurations, with the estimated values able to capture in an excellent way the experimental data almost in the whole range of variation of the drift angle. Overall, for this configuration, the non-linear part is also predicted with an acceptable accuracy.

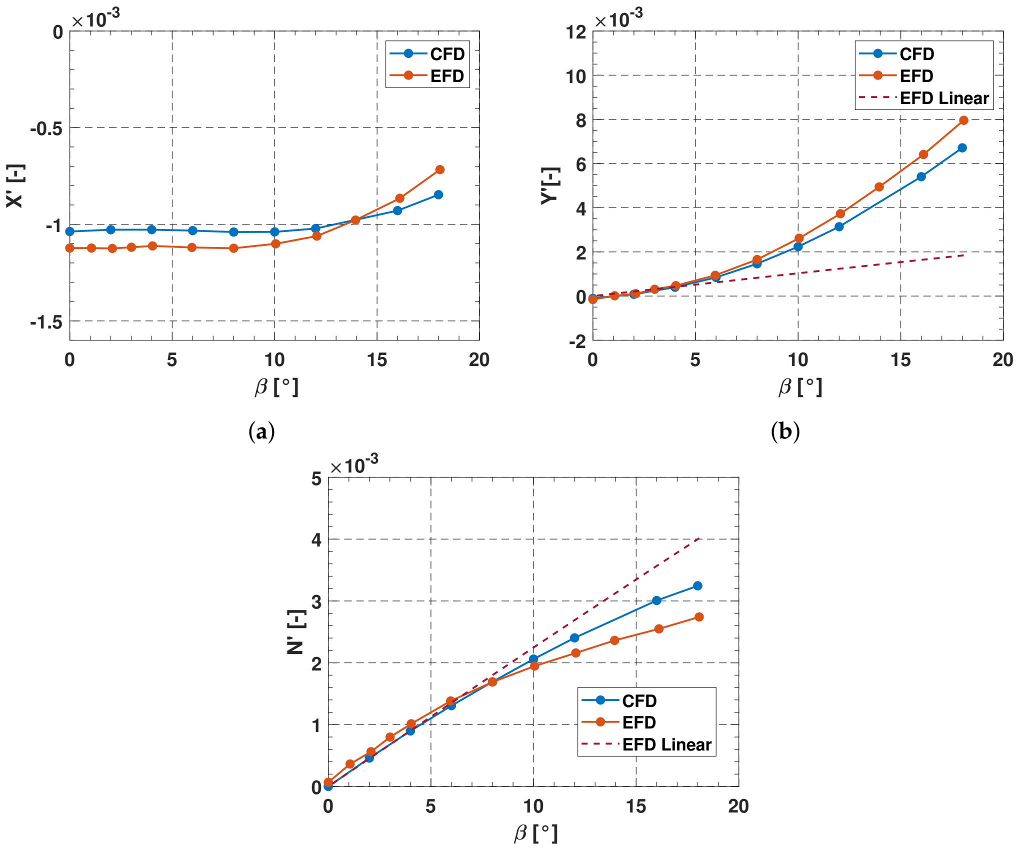

Figure 24. Comparison between numerical results (blue) and experimental data (orange) of X' (**a**), Y' (**b**) and N' (**c**) for the barehull with ring wing configuration. The linear component is shown with dashed red line.

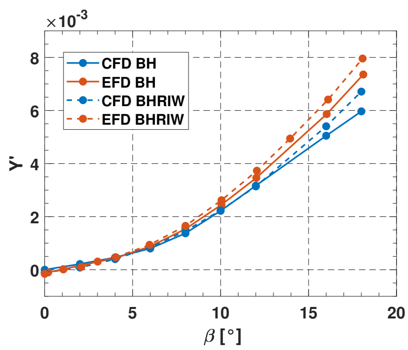

Figure 25. Increment of the lateral force for both the numerical simulation (blue) and the experimental data (orange) due to the presence of the ring wing.

From this standpoint, the significant improvement in the results could be related to the presence of the rudders and sternplane surfaces. The stern appendages have an impact on the pressure fields in that region, reducing the influence and the intensity of the streamwise vortices generated in the barehull configuration. In Figure 27, the vortices generated on the two configurations are compared.

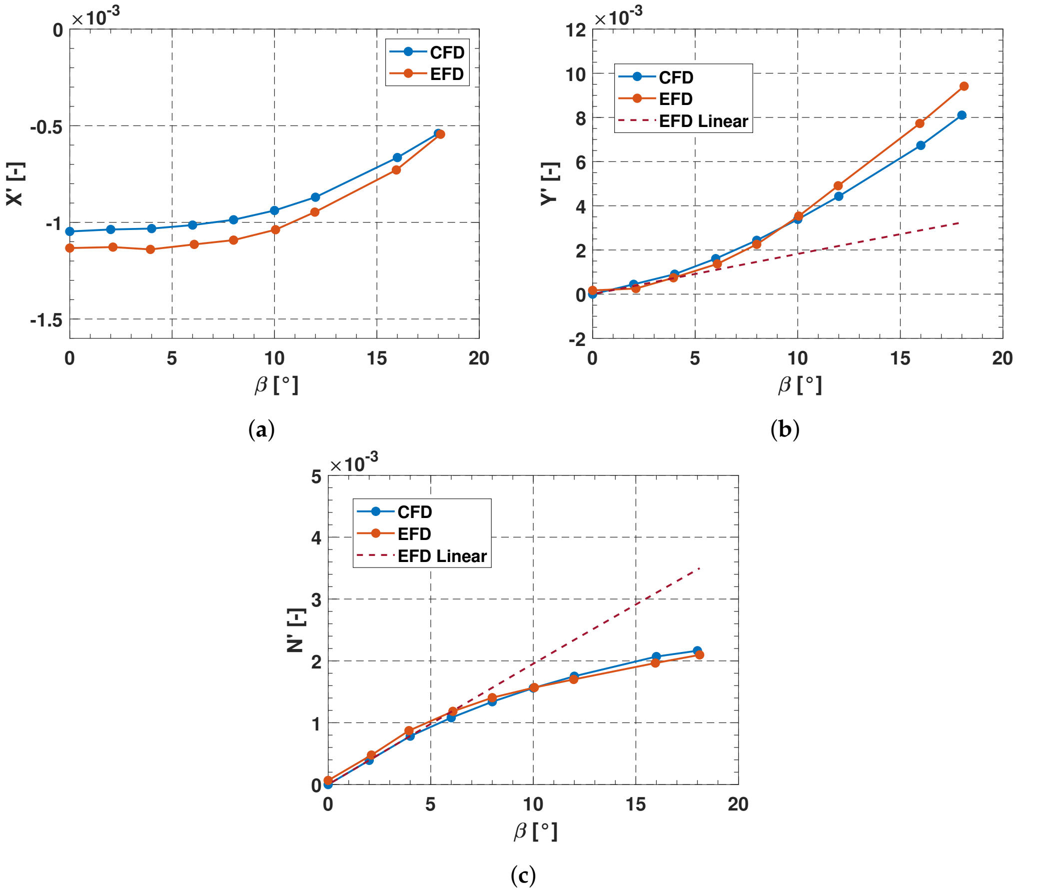

Figure 26. Comparison between numerical results (blue) and experimental data (orange) of X' (**a**), Y' (**b**) and N' (**c**) for the barehull with stern appendages configuration. The linear component is shown with dashed red line.

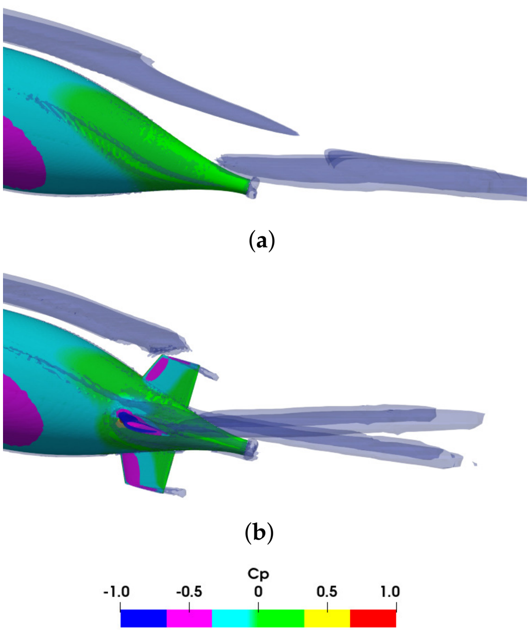

Figure 27. Iso-surface of Q, hull coloured by pressure coefficient magnitude for two different configurations BH (**a**) and $BHSTAP$ (**b**).

A further investigation is illustrated in Figure 28, considering the sectional forces already defined in Section 5.1. The non-dimensional coefficient of the lateral force for both configurations, BH in blue and $BHSTAP$ in orange, are compared along the submarine. The reduction in the negative lateral force can be noticed in the stern region where the appendages are present. In this way, the previously mentioned error becomes less important in the definition of the overall hull lateral force and yaw moment, improving, consequently, the agreement with experiments.

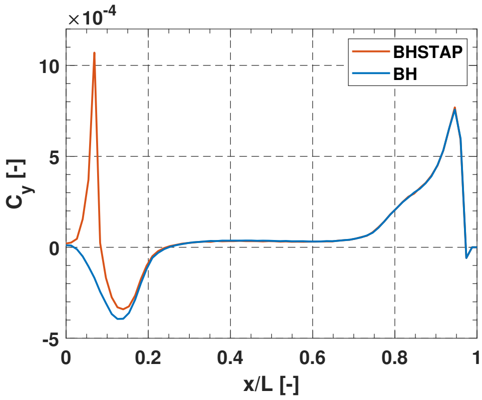

Figure 28. Comparison between the lateral forces for the two different configurations: BH (blue) and $BHSTAP$ (orange) for 16° drift angle. C_y is the lateral force coefficient.

4.4. Barehull with Sail

As in the previous cases, a good agreement with the experimental data can be noticed from Figure 29 when the sail is included in the analyses. However, a limitation of RANS CFD simulations becomes manifest in the early-stalling phenomenon of the sail (and airfoils in general, as shown in similar cases in [29,52]). For this reason, Figure 29b shows with a purple line (with triangular marks) the impact of the linearization of the sail contribution on the total lateral force, neglecting the possibly erroneous non-linear stall prediction. Linearization is obtained following the procedure devised in Franceschi et al. [29]. With this assumption, the total value of the lateral force acting on the submarine is predicted with a higher accuracy.

As the reference system is that of the hull, in Figure 30, the total axial force is projected in the direction of the drag and the lateral force acting on the sail in that of lift. It is clear how after the 10° of drift angle, the lateral force acting on the sail drops, losing its linear trend, clearly indicating the sail stall. At the same angle, in Figure 29a, where the X' force is shown, the trend of the predicted force changes, compared to the experimental one, and starts decreasing earlier, whereas this occurs at 16° for the experimental data. Without the experimental values for the forces acting on the sail, the previous facts can lead to the hypothesis that at drift angle 16°, the sail stalls experimentally, showing also the influence of the sail stall on the longitudinal force. The axial force when projected in the drag direction continues increasing after the stall point, as expected for an airfoil; this is a phenomenon that cannot be appreciated in Figure 29.

The virtual stalling of the sail can be visualized also in Figure 31, where, as in the previous section, the Q-factor was used to visualize the location of the vortices and the stalling of the sail. For the two considered angles (16° and 18°), the sail tip vortex is reduced and a vast region on the back of the profile is covered by a strong recirculation phenomenon. This behaviour shows the presence of a stalled profile. It is interesting to note that in the previous section, when the rudders and the sternplanes are considered, no stall phenomena were mentioned. This different behaviour can be ascribed to the straightening flow effect induced by the hull in its stern region, which reduces the effective rudder angle to the lifting surfaces.

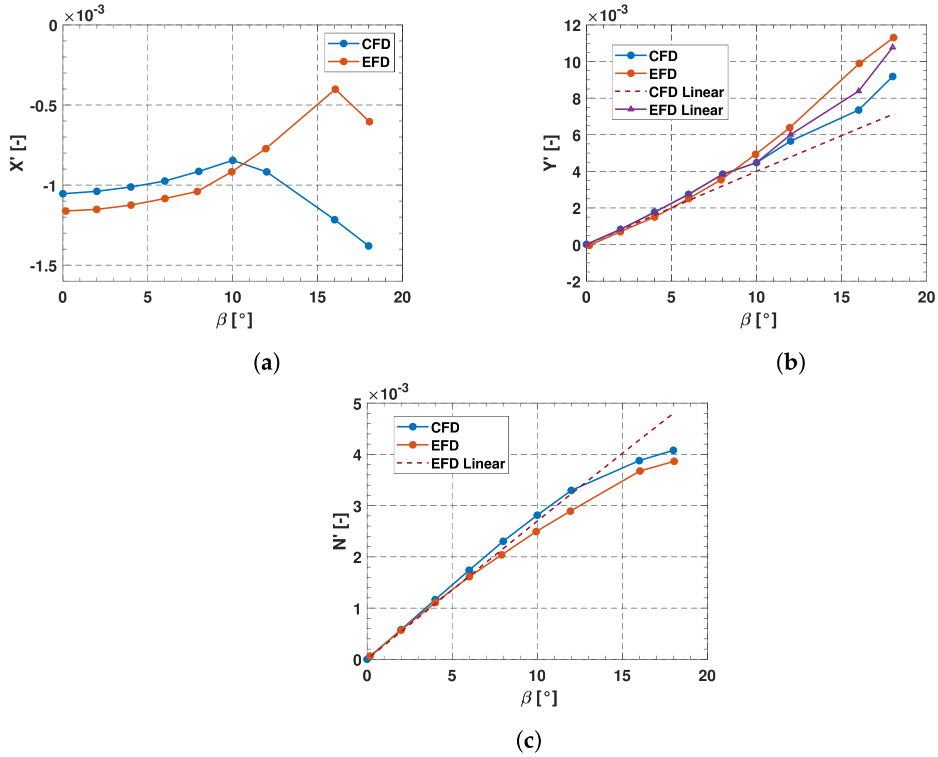

Figure 29. Comparison between numerical results (blue) and experimental data (orange) of X' (**a**), Y' (**b**) and N' (**c**) for the barehull with sail configuration. The linear component is shown with dashed red line.

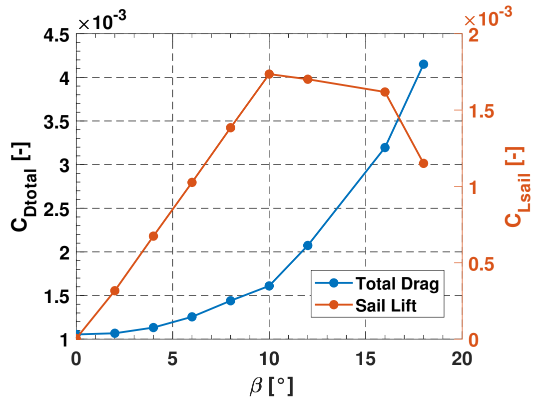

Figure 30. Projected total drag and projected sail lift.

With all the above in mind, the quality of the simulations can be anyway considered satisfactory as a practical compromise between computational effort and accuracy. This is in line with the aim of CFD-based captive model tests, which are used to extract data (as the hydrodynamic coefficients) to be adopted in a lumped parameter simulator [54].

4.5. Fully Appended Configuration

The fully appended results are summarized in Figure 32. As in the configuration with the sail, in this case the trend of the CFD simulation data also shows that the sail still stalls at smaller drift angles with respect to the experimental evidence. Nonetheless, in this configuration, which is also the operating configuration of a real underwater vehicle, there is a very good agreement between calculations and experiments. This may be naturally explained according to the huge relevance and lift effectiveness of the stern rudders and planes in terms of manoeuvring forces with respect to the slender hull and sail shapes. A satisfactory matching of the lateral force and yaw moment can be observed, especially for smaller drift angles. As mentioned before, the sail stalling occurs earlier for the CFD predictions compared to the experimental data.This gives us a hint that the discrepancy between the experimental and the predicted values of the longitudinal force X, for angles greater than 10° (which is the same angle of the numerical stalling of the sail), may be caused by this exact phenomenon. Of interest for further investigation is the case in which the numerically obtained lift of the sail continues its linear trend, and thus a projected contribution of the force on the x-axis is present. Nonetheless compared to the barehull with sail configuration the differences in the Y and N components in this case are relatively less relevant due to the high influence of the stern appendages. The CFD modelling deficiency remains evident in terms of longitudinal force according to the sudden drop of the lift induced quadratic drag.

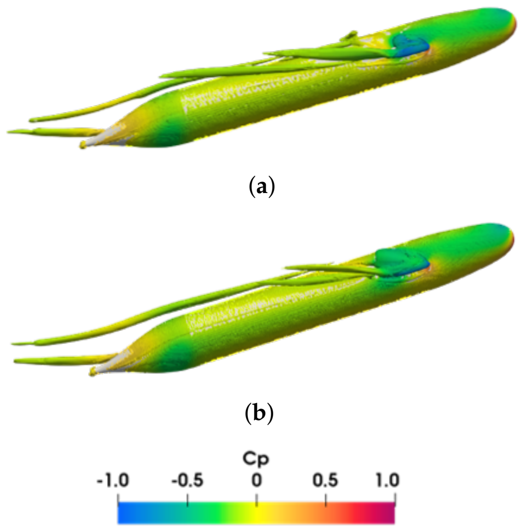

Figure 31. Iso-surface of Q by the pressure coefficient magnitude for two different drift angles $\beta = 16°(a), 18°$ (b), for the BHS configuration.

In addition to the in-plane manoeuvring forces and moments, the out-of-plane components were also investigated, with an eye to the so-called stern dipping phenomenon [55,56]. Figure 33 shows the comparison between the predicted and the measured out-of-plane force Z', roll moment K', and pitch moment M' acting on the fully appended submarine owing to the horizontal drift attitude. The out-of-plane loads are due to the lifting properties of the sail, which, owing to the tip vortex shedding, induce a crossflow braking element of the circulation around the hull aft the sail. This reduces the average crossflow velocity above the hull, thus increasing the pressure, and generates a stern down force. It is evident from the figure that the CFD simulations are successful in describing both the trend and the values of the experimental data, especially for small drift angles. The stall of the sail can be still observed in terms of roll moment drop.

For the fully appended configuration, apart from horizontal drift angle, tests with vertical drift angle (angle of attack) were also conducted. In Figure 34, the predicted forces X', Z' and moment M' about the y-axis are compared to the experimental data. It should be recalled that, in this case, the sail is a symmetry-braking element, but it is not acting as a lifting surface, and thus early stall issues are expected to be eliminated; the test matrix considers both the positive and negative angle of attack in order to capture the above mentioned asymmetry, even if minor differences are visible. In this case, no particular differences can be observed in terms of longitudinal force X', due to the non-lifting condition of the sail; the initial drag bias is maintained all over the drift range, with discrepancies increasing at higher drift angles. The Z' and M' the predictions satisfactorily match the experiments until 10°. The linear part of the experimental measurements, shown in the graphs with the red dashed line, is well captured by the CFD simulations as it is evident from Figure 34b,c. The non-linear discrepancies at the higher angles could be ascribed to the previously mentioned problem of the pressure recovery in the stern region; in fact, the numerical/experimental gap is of the same order and behaviour of the one shown for the barehull with only rudder configuration.

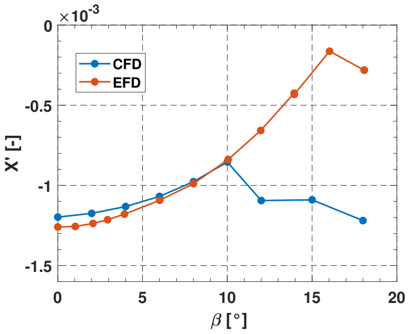

(**a**)

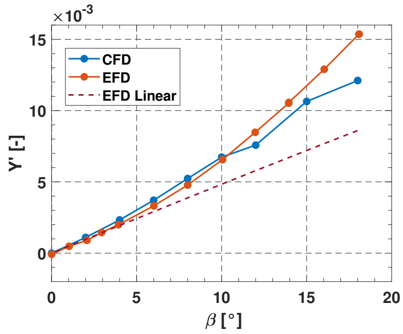

(**b**)

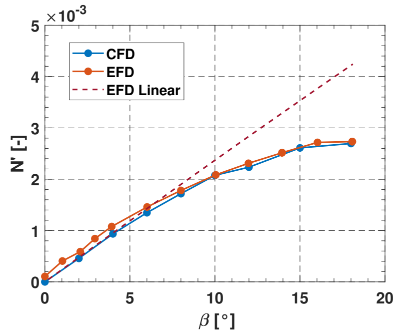

(**c**)

Figure 32. Horizontal plane. Comparison between numerical results (blue) and experimental data (orange) of X' (**a**), Y' (**b**) and N' (**c**) for the fully appended configuration. The linear component is shown with dashed red line.

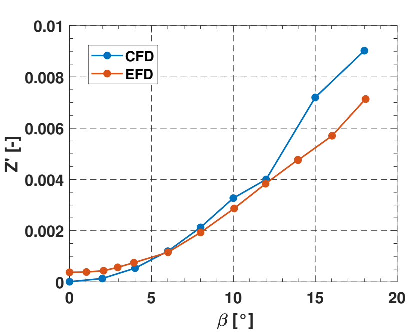

(**a**)

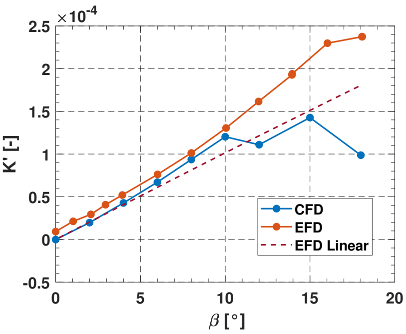

(**b**)

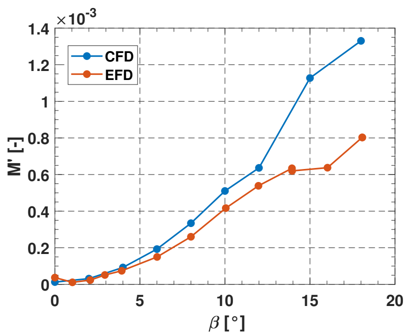

(**c**)

Figure 33. Out-of-plane components for the *FA* configuration with several drift angles; (**a**) vertical force; (**b**) rolling moment; (**c**) pitching moment

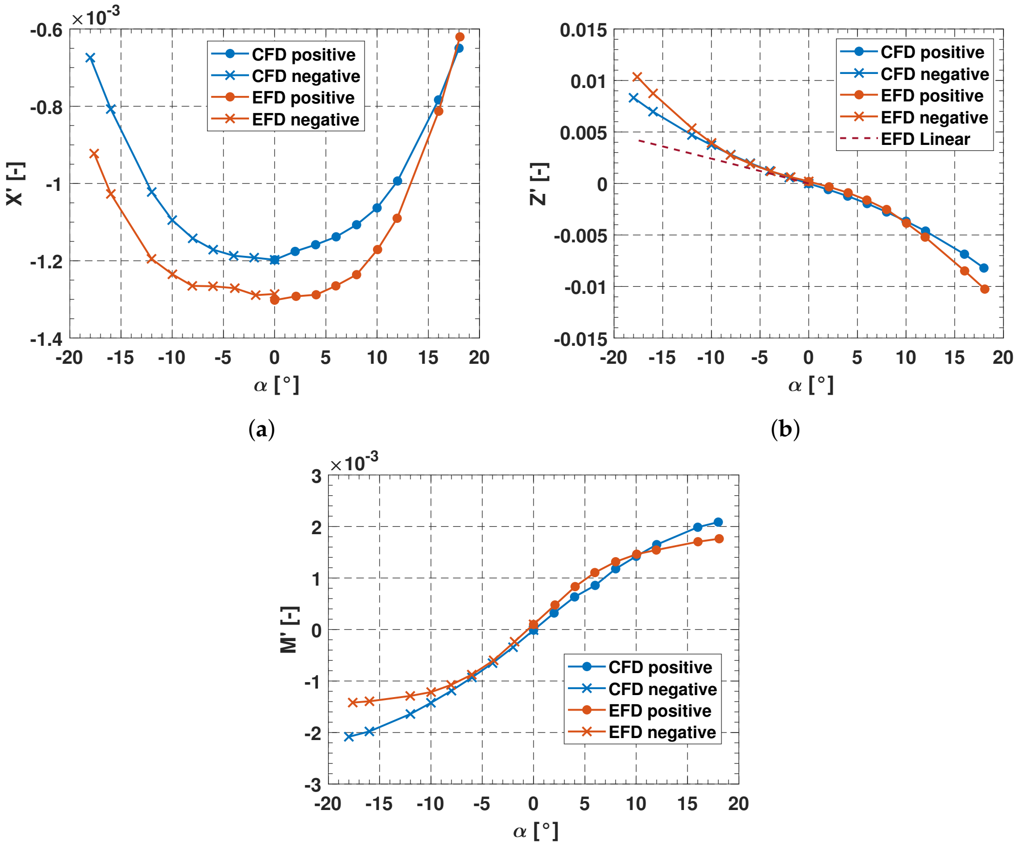

(**a**) (**b**) (**c**)

Figure 34. Vertical plane. Comparison between numerical results (blue) and experimental data (orange) of X' (**a**), Z' (**b**) and M' (**c**) for the fully appended configuration. The linear component is shown with dashed red line.

5. Results: Rudder Tests—Fully Appended Configuration

In Figure 35, the results of the rudder tests conducted at DTRC and the CFD simulations are set side by side. The experimental tests include both the total forces acting on the fully appended submarine with rudder δ_r or sternplane angles δ_s (Figure 35), as well as those acting on the single fin (Figure 36). Pressure taps were installed in the upper rudder and the sternplane rudder, thus enabling the verification of the wing–body interactions according to the CFD methodologies.

Both positive and negative angles were investigated by DTRC but given the symmetry of the submarine in the horizontal plane, the outcomes of the two measurements should theoretically match. The remaining differences between the outcomes of the two ranges might be considered an estimation of experimental uncertainty.

From Figure 35, it can be noticed how the simulation results fall within that uncertainty, both in terms of longitudinal X' and steering force Y'. Overall, the trend of the experimental outcomes is well captured by the CFD simulations. By looking at the single upper rudder measurements, reported in Figure 36, a good correspondence is visible, allowing a satisfactory validation of the methodology. It is quite curious that the value of the X' force for 5° of rudder angle is very similar to the case of no rudder angle. For the sake of the direct comparison between the predicted and the measured forces acting on the rudders, the former values were rotated from the body frame of reference to the normal and chordwise directions of the control surface, where the measurements were conducted. The rotation of such values might be the possible justification for the values of the longitudinal force on the upper rudder for $\delta_R = 5°$. Anyway, the most important force component during a manoeuvre is the lateral one, which is accurately predicted. This rotation has an impact also on the Y' force, but its magnitude is negligible, compared to that on X'.

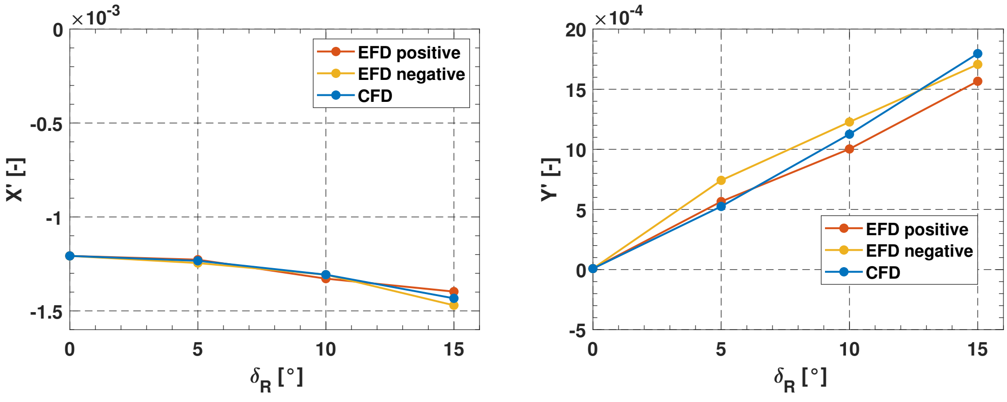

(**a**) (**b**)

Figure 35. Comparison between the numerically estimated values and the experimental data of the acting forces X' (**a**), and Y' (**b**) on the fully appended configuration for different rudder angles (δ). Experimental data for both positive (orange) and negative (yellow) rudder angles.

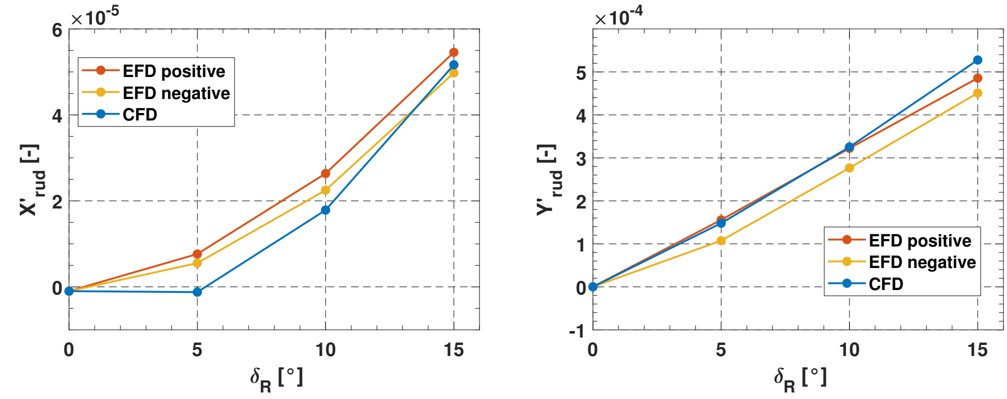

(**a**) (**b**)

Figure 36. Comparison between the numerically estimated values and the experimental data of the forces X'_{rudder} (**a**), and Y'_{rudder} (**b**), acting on the upper rudder of the fully appended configuration for different rudder angles (δ_R).

According to the previous observations, an interesting aspect of the investigation concerns the evaluation of the wing–body interaction at the stern. This can be studied according to the comparison between the total forces acting on the submarine and the isolated sum of those on the upper and lower rudders. Figure 37 shows in orange the sum of the lateral forces on the upper and the lower rudder and in blue the total lateral force on the submarine (both values are from CFD calculations).

This figure clearly shows how the pressure field on the stern appendages has an impact on the hull as well, leading to the generation of lateral forces on it. This amplification phenomenon is well known in the literature, especially in the case of small stern body radii with respect to the wing planform [54,57,58]. In the current analysed case, these hull amplification forces account for about 50% of the rudder forces. Therefore, the phenomenon heavily affects the manoeuvring in terms of global control forces; the correct capturing of this aspect is thus fundamental for the early design stage study of an underwater vehicle.

Switching to the vertical manoeuvring plane, Figure 38 and Figure 39 show, respectively, the total forces X' and Z' relevant to the stern planes execution, as well as the X'_{rudder} and Z'_{rudder} referring to the forces acting on the portside sternplane alone. The prediction of the longitudinal force shows a better accuracy in terms of global force with respect to the single fin case, whereas the vertical force has a good accuracy for both cases. Again, the overall trend of the experimental data is well described by the simulation outcomes.

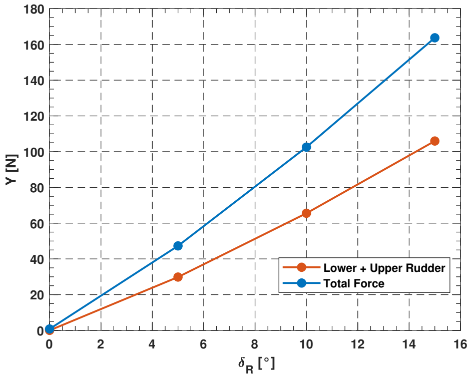

Figure 37. Comparison between the sum of the lateral forces acting on the two rudders (orange) and the total lateral force acting on the submarine (blue) for the *FA* configuration.

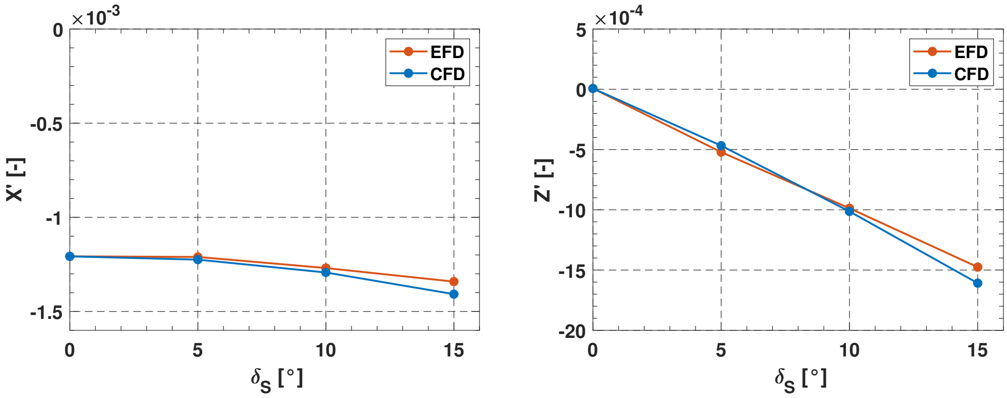

(**a**) (**b**)

Figure 38. Comparison between the numerically estimated values and the experimental data of the acting forces X'_{rudder} (**a**), and Z'_{rudder} (**b**), on the fully appended configuration for different sternplane angles (δ_S).

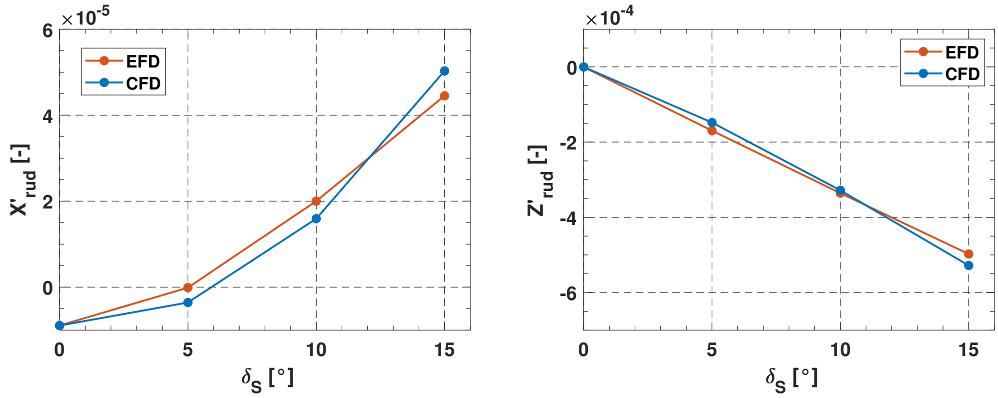

(**a**) (**b**)

Figure 39. Comparison between the numerically estimated values and the experimental data of the forces X'_{rudder} (**a**), and Z'_{rudder} (**b**), acting on the portside sternplane of the fully appended configuration for different sternplane angles (δ_S).

Also, in this case, the total vertical force Z is higher than the sum of the vertical forces acting on the sternplanes, as reported in Figure 40, with a similar amplification factor.

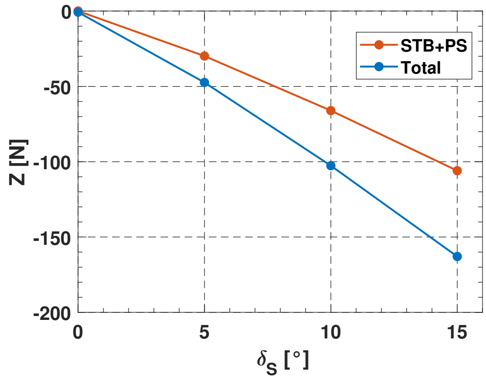

Figure 40. Comparison between the sum of the vertical forces acting on the two rudders (orange) and the total vertical force acting on the submarine (blue) for the *FA* configuration.

Finally, combined rudder and drift tests were considered, as reported in Figure 41. The values of the forces measured by simulations have the same trend observed in experiments, and the linear behaviour of the combined tests is well predicted. The discrepancies between the predicted and the measured data, for 0°, are those already discussed, even though in this illustration they appear more marked. Considering the aim of the captive model tests, the rudder hydrodynamic derivatives are well captured, no matter the reported discrepancies when the rudder angle is zero.

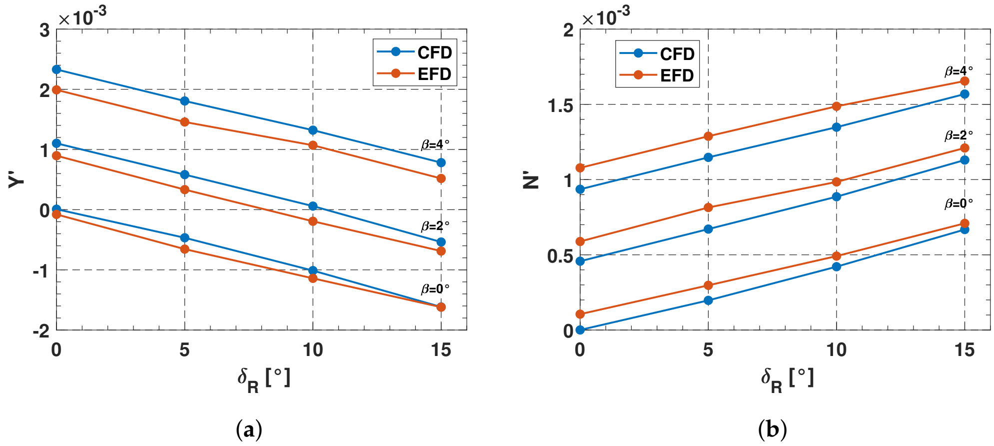

Figure 41. Comparison between predicted and experimentally measured values of non-dimensional lateral force Y'_{rudder} (**a**), and moment N'_{rudder} (**b**), for *FA* configuration, for different drift angles (β) and rudder angles (δ_R).

5.1. Results: Pure Rotation

CFD predictions were also carried out for the pure rotation case. Both the vertical and the horizontal plane cases were investigated. The results are compared with the angular velocity derivatives reported in Roddy [22]. Unfortunately, complete experimental measurements were not available for a systematic comparison, and only linear trends were considered. Figure 42 and Figure 43 (for the horizontal and vertical plane, respectively) show the results obtained from the numerical simulations (in blue) compared to the experimental data (in orange). Small differences between the predicted values and the pure linear trend obtained by the derivative can be noted for the moments N' and M' and for the vertical force Z'. The vertical force and the two moments, differently from the lateral force, are characterized by limited nonlinear parts. Globally, the overall agreement is very good also for the rotation cases. This, furthermore, enhances the reliability of the proposed numerical procedure to feed a manoeuvring simulator for UVs.

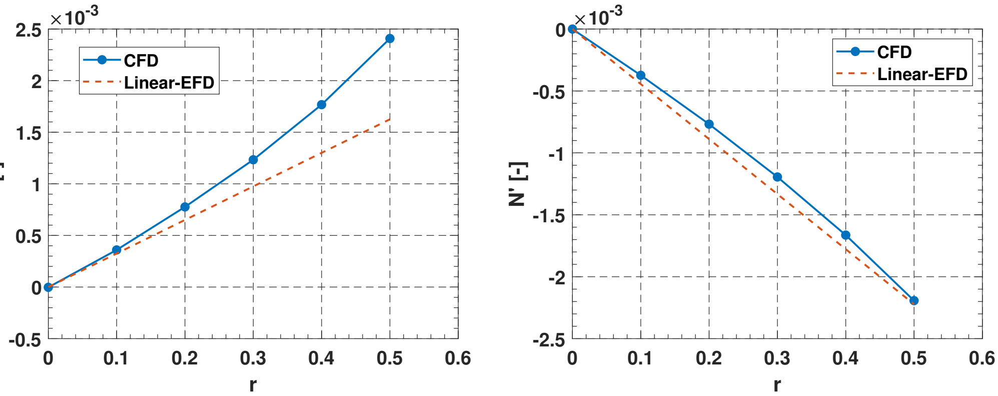

(a) (b)

Figure 42. Comparison between CFD predictions and the experimental data for different angular velocity values in the horizontal plane; (**a**) lateral force; (**b**) yaw moment.

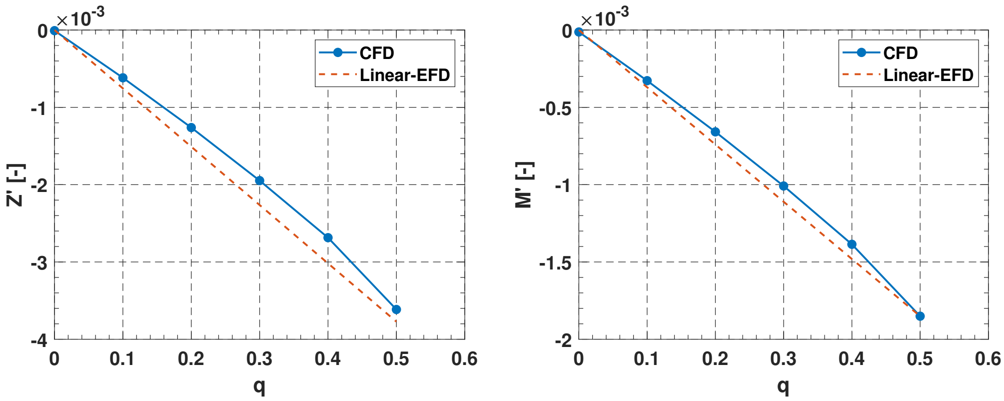

(a) (b)

Figure 43. Comparison between CFD predictions and the experimental data for different angular velocity values in the vertical plane; (**a**) vertical force; (**b**) pitching moment.

6. Conclusions

In the current study, an extensive validation of RANS methodologies for the prediction of the hydrodynamic coefficients of the DARPA SUBOFF in five different configurations, corresponding to BH, BHS, BHSTAP, BHRIW, and FA underwater vehicles, is presented. Pure drift and rotation tests (in the horizontal and vertical plane) were investigated, as well as pure rudder or sternplate angles tests and some combined drift and rudder tests, consistently with captive model experiments conducted by DTRC [22]. The aim of this study was to consolidate the reliability of the CFD simulations to predict the hull and the appendages forces during a manoeuvre of underwater vehicles with an eye to a modular approach of each single hydrodynamic component.

The open-source OpenFOAM software was successfully employed. Three different meshes were used to verify the grid sensitivity, showing a good convergent trend of the global forces already with a quite low demanding mesh arrangement of about 3 million cells, representing a good compromise between the computational time and the accuracy of the results. The expected uncertainty for the most important manoeuvring forces is within 2%, with a slightly lower performance for the fully appended configuration about 3%.

The results of the horizontal and vertical drift and rotation cases showed an overall good agreement with the experimental data. The linear part is captured in an excellent way from the results of the simulations in all the horizontal and vertical plane cases, considering both in- and out-of plane components (the latter generated by the sail effect). Regarding the barehull configuration, two streamwise vortices were noticed to have an important impact on the non-linearities present in the bare hull results in the drifting attitudes, when the stern appendages are not installed. An increment of the lateral force for both experimental and numerical results occurs when the ring wing is present. The stall of the sail when dealing with the barehull with sail configuration occurs numerically earlier than in the experiments (approximately at 10°); this might be the cause of the discrepancies in the longitudinal force. Further investigation is needed in this direction. These differences are present also in the fully appended configuration; however, compared to the barehull with sail case, these are relatively less relevant due to the high influence of the stern appendage. Nevertheless, the X force, when dealing with manoeuvring simulators, is not so relevant as most of the time, it is calculated separately. The numerical results for the rudder tests capture well the trend of the experiments, enabling the assessment of the control forces, including the hull–wing amplification interactions. This aspect is worth studying deeply in further research; in fact, it has a significant impact on the manoeuvring ability of a submerged vehicle.

The expected errors between the measured data and the predictions for the fully appended configuration are within 5% for the linear part and 15% for the higher drift angles. From an engineering point of view, this makes the approach reliable, as the operating configuration of a submarine is the fully appended one. In conclusion, the proposed numerical methodology allows a proper assessment of both the linear stability and controllability features of an underwater vehicle with respect to both the manoeuvring planes. Further investigation is needed in order to build high confidence in such methods for the early-stage design of an underwater vehicle, especially in the wider nonlinear ranges of motion. Different turbulence models should be investigated in order to better capture and describe the generated vortices while manoeuvring, especially for the barehull configuration. This further analysis requires the availability of more experimental data on different geometries.

Author Contributions: Conceptualization, D.V., B.P., S.G. and M.V.; methodology, D.V., B.P., S.G. and M.V.; data curation, V.V.Z.; writing—original draft, V.V.Z.; writing—review and editing, D.V., B.P., S.G. and M.V. All authors have read and agreed to the published version of the manuscript.

Funding: This research received no external funding.

Institutional Review Board Statement: Not applicable.

Informed Consent Statement: Not applicable.

Data Availability Statement: Data are contained within the article.

Conflicts of Interest: The authors declare no conflict of interest.

References

1. Lin, Y.H.; Tseng, S.H.; Chen, Y.H. The experimental study on maneuvering derivatives of a submerged body SUBOFF by implementing the Planar Motion Mechanism tests. *Ocean Eng.* **2018**, *170*, 120–135. [CrossRef]
2. Renilson, M. *Submarine Hydrodynamics*; Springer: Berlin/Heidelberg, Germany, 2015; Volume 31.
3. Hoyt, E.D.; Imlay, F.H.; David Taylor Model Basin Washington DC. *The Influence of Metacentric Stability on the Dynamic Longitudinal Stability of a Submarine SRD 542/46 NS 512-001*; David Taylor Model Basin Washington DC: Washington, DC, USA, 1948.
4. Anderson, B.; Chapuis, M.; Erm, L.; Fureby, C.; Giacobello, M.; Henbest, S.; Jones, D.; Jones, M.; Kumar, C.; Liefvendahl, M.; et al. Experimental and computational investigation of a generic conventional submarine hull form. In Proceedings of the 29th Symposium on Naval Hydrodynamics, Gothenburg, Sweden, 26–31 August 2012.
5. Quick, H.; Widjaja, R.; Anderson, B.; Woodyatt, B.; Snowden, A.D.; Lam, S. *Phase I Experimental Testing of a Generic Submarine Model in the DSTO Low Speed Wind Tunnel*; Client Report, DSTO-TN-1101; Defence Science and Technology Organisation: Victoria, Australia, 2012.
6. Fureby, C.; Anderson, B.; Clarke, D.; Erm, L.; Henbest, S.; Giacobello, M.; Jones, D.; Nguyen, M.; Johansson, M.; Jones, M.; et al. Experimental and numerical study of a generic conventional submarine at 10 yaw. *Ocean Eng.* **2016**, *116*, 1–20. [CrossRef]
7. Dubbioso, G.; Broglia, R.; Zaghi, S. CFD analysis of turning abilities of a submarine model. *Ocean Eng.* **2017**, *129*, 459–479. [CrossRef]
8. Broglia, R.; Posa, A.; Bettle, M.C. Analysis of vortices shed by a notional submarine model in steady drift and pitch advancement. *Ocean Eng.* **2020**, *218*, 108236. [CrossRef]
9. Lee, S.K.; Manovski, P.; Kumar, C. Wake of a cruciform appendage on a generic submarine at 10 yaw. *J. Mar. Sci. Technol.* **2020**, *25*, 787–799. [CrossRef]

10. Wackers, J.; Deng, G.; Guilmineau, E.; Leroyer, A.; Queutey, P.; Visonneau, M. What is happening around the KVLCC2? In Proceedings of the 18th Numerical Towing Tank Symposium (NuTTS 2015), Cortona, Italy, 28–30 September 2015.
11. Zhang, Z.; Guo, L.; Wei, P.; Wang, X.; Feng, D. Numerical simulation of submarine surfacing motion in regular waves. *Iran. J. Sci. Technol. Trans. Mech. Eng.* **2020**, *44*, 359–372. [CrossRef]
12. Posa, A.; Balaras, E. A numerical investigation of the wake of an axisymmetric body with appendages. *J. Fluid Mech.* **2016**, *792*, 470–498. [CrossRef]
13. Morse, N.; Mahesh, K. Large-eddy simulation and streamline coordinate analysis of flow over an axisymmetric hull. *J. Fluid Mech.* **2021**, *926*, A18. [CrossRef]
14. Rocca, A.; Cianferra, M.; Broglia, R.; Armenio, V. Computational hydroacoustic analysis of the BB2 submarine using the advective Ffowcs Williams and Hawkings equation with wall-modeled LES. *Appl. Ocean Res.* **2022**, *129*, 103360. [CrossRef]
15. Lungu, A. DES-based computation of the flow around the DARPA suboff. In Proceedings of the IOP Conference Series: Materials Science and Engineering, Kazimierz Dolny, Poland, 21–23 November 2019; Volume 591, p. 012053.
16. Lungu, A. Large flow separations around a generic submarine in static drift motion resolved by various turbulence closure models. *J. Mar. Sci. Eng.* **2022**, *10*, 198. [CrossRef]
17. Wang, L.; Martin, J.; Carrica, P.; Felli, M.; Falchi, M. Experiments and CFD for DARPA suboff appended with propeller E1658 operating near the surface. In Proceedings of the 6th International Symposium on Marine Propulsors, Rome, Italy, 26–30 May 2019; pp. 1–9.
18. Wang, L.; Martin, J.E.; Felli, M.; Carrica, P.M. Experiments and CFD for the propeller wake of a generic submarine operating near the surface. *Ocean Eng.* **2020**, *206*, 107304. [CrossRef]
19. Guo, H.; Li, G.; Du, L. Investigation on the flow around a submarine under the rudder deflection condition by using URANS and DDES methods. *Appl. Ocean Res.* **2023**, *131*, 103448. [CrossRef]
20. Jones, D.A.; Clarke, D.B.; Brayshaw, I.B.; Barillon, J.L.; Anderson, B. *The Calculation of Hydrodynamic Coefficients for Underwater Vehicles*; Technical Report; Defense Technical Information Center: Fort Belvoir, VA, USA, 2002.
21. Groves, N.C.; Huang, T.T.; Chang, M.S. *Geometric Characteristics of DARPA Suboff Models: (DTRC Model Nos. 5470 and 5471)*; David Taylor Research Center: Bethesda, MD, USA, 1989.
22. Roddy, R.F. *Investigation of the Stability and Control Characteristics of Several Configurations of the DARPA SUBOFF Model (DTRC Model 5470) from Captive-Model Experiments*; DTRC/SHD-1298-08; David Taylor Research Center, Ship Hydromechanics Department: Bethesda, MD, USA, 1990.
23. Huang, T.T.; Liu, H.L.; Groves, N.C. *Experiments of the Darpa (Defense Advanced Research Projects Agency) Suboff Program*; David Taylor Research Center, Ship Hydromechanics Department: Bethesda, MD, USA, 1989.
24. Joubert, P. *Some Aspects of Submarine Design: Part 1: Hydrodynamics*; Australian Department of Defence: Canberra, Australia, 2004.
25. Joubert, P. *Some Aspects of Submarine Design. Part 2. Shape of a Submarine 2026*; Technical Report; Australian Department of Defence: Canberra, Australia, 2006.
26. Overpelt, B.; Nienhuis, B.; Anderson, B. Free running manoeuvring model tests on a modern generic SSK class submarine (BB2). In Proceedings of the Pacific International Maritime Conference, Sydney, Australia, 6–8 October 2015; pp. 1–14.
27. Du, P.; Cheng, L.; Tang, Z.j.; Ouahsine, A.; Hu, H.b.; Hoarau, Y. Ship maneuvering prediction based on virtual captive model test and system dynamics approaches. *J. Hydrodyn.* **2022**, *34*, 259–276. [CrossRef]
28. Franceschi, A.; Piaggio, B.; Villa, D.; Viviani, M. Development and assessment of CFD methods to calculate propeller and hull impact on the rudder inflow for a twin-screw ship. *Appl. Ocean Res.* **2022**, *125*, 103227. [CrossRef]
29. Franceschi, A.; Piaggio, B.; Tonelli, R.; Villa, D.; Viviani, M. Assessment of the Manoeuvrability Characteristics of a Twin Shaft Naval Vessel Using an Open-Source CFD Code. *J. Mar. Sci. Eng.* **2021**, *9*, 665. [CrossRef]
30. Piaggio, B.; Villa, D.; Viviani, M. Numerical analysis of escort tug manoeuvrability characteristics. *Appl. Ocean Res.* **2020**, *97*, 102075. [CrossRef]
31. Weller, H.G.; Tabor, G.; Jasak, H.; Fureby, C. A tensorial approach to computational continuum mechanics using object-oriented techniques. *Comput. Phys.* **1998**, *12*, 620–631. [CrossRef]
32. Versteeg, H.K.; Malalasekera, W. *An Introduction to Computational Fluid Dynamics: The Finite Volume Method*; Pearson Education: Upper Saddle River, NJ, USA, 2007.
33. Wilcox, D.C. *Turbulence Modeling for CFD*; DCW Industries: La Canada, CA, USA, 1998; Volume 2.
34. Menter, F.R. Two-equation eddy-viscosity turbulence models for engineering applications. *AIAA J.* **1994**, *32*, 1598–1605. [CrossRef]
35. Launder, B.E.; Spalding, D.B. *Lectures in Mathematical Models of Turbulence*; Academic Press: London, UK; New York, NY, USA, 1972; 169p.
36. Spalding, D.B. The numerical computation of turbulent flow. *Comp. Methods Appl. Mech. Eng.* **1974**, *3*, 269.
37. Shih, T.H.; Liou, W.W.; Shabbir, A.; Yang, Z.; Zhu, J. A new k-epsilon eddy viscosity model for high reynolds number turbulent flows. *Comput. Fluids* **1995**, *24*, 227–238. [CrossRef]
38. Juretic, F. *cfMesh User Guide*; Creative Fields, Ltd.: London, UK, 2015; Volume 1.
39. Zheku, V.; Villa, D.; Gaggero, S. A Detailed Analysis of Manoeuvring Performance of Solid of Revolutions. In Proceedings of the MARINE Conference, Madrid, Spain, 27–29 June 2023.

40. Kim, H.; Leong, Z.Q.; Ranmuthugala, D.; Forrest, A. CFD modelling and validation of an AUV undergoing variable accelerations. In Proceedings of the ISOPE International Ocean and Polar Engineering Conference, Busan, Republic of Korea, 15–20 June 2014; p. ISOPE-I.
41. Pan, Y.C.; Zhang, H.X.; Zhou, Q.D. Numerical prediction of submarine hydrodynamic coefficients using CFD simulation. *J. Hydrodyn.* **2012**, *24*, 840–847. [CrossRef]
42. Amiri, M.M.; Esperança, P.T.; Vitola, M.A.; Sphaier, S.H. An initial evaluation of the free surface effect on the maneuverability of underwater vehicles. *Ocean Eng.* **2020**, *196*, 106851. [CrossRef]
43. Amiri, M.M.; Esperança, P.T.; Vitola, M.A.; Sphaier, S.H. How does the free surface affect the hydrodynamics of a shallowly submerged submarine? *Appl. Ocean Res.* **2018**, *76*, 34–50. [CrossRef]
44. Dawson, E. An Investigation into the Effects of Submergence Depth, Speed and Hull Length-to-Diameter Ratio on the near Surface Operation of Conventional Submarines. Ph.D. Thesis, University of Tasmania, Hobart, Australia, 2014.
45. Celik, I.B.; Ghia, U.; Roache, P.J.; Freitas, C.J. Procedure for estimation and reporting of uncertainty due to discretization in CFD applications. *J. Fluids Eng.-Trans. ASME* **2008**, *130*. [CrossRef]
46. Roache, P.J. Quantification of uncertainty in computational fluid dynamics. *Annu. Rev. Fluid Mech.* **1997**, *29*, 123–160. [CrossRef]
47. Hoang, N.; Wetzel, T.; Simpson, R. Unsteady measurements over a 6: 1 prolate spheroid undergoing a pitch-up maneuver. In Proceedings of the 32nd Aerospace Sciences Meeting and Exhibit, Reno, NV, USA, 10–13 January 1994; p. 197.
48. Kotapati-Apparao, R.B.; Squires, K.D. Prediction of a prolate spheroid undergoing a pitchup maneuver. In Proceedings of the 41 st AIAA Aerospace Sciences Meeting & Exhibit, Reno, NV, USA, 6–9 January 2003.
49. Subrahmanya, M.; Rajani, B. Numerical Investigation of the Flow Past 6: 1 Prolate Spheroid. 2019.
50. Chesnakas, C.J.; Simpson, R.L. Detailed investigation of the three-dimensional separation about a 6: 1 prolate spheroid. *AIAA J.* **1997**, *35*, 990–999. [CrossRef]
51. Jeong, J.; Hussain, F. On the identification of a vortex. *J. Fluid Mech.* **1995**, *285*, 69–94. [CrossRef]
52. Villa, D.; Gaggero, S.; Tani, G.; Viviani, M. Numerical and experimental comparison of ducted and non-ducted propellers. *J. Mar. Sci. Eng.* **2020**, *8*, 257. [CrossRef]
53. Andersson, J.; Eslamdoost, A.; Vikström, M.; Bensow, R.E. Energy balance analysis of model-scale vessel with open and ducted propeller configuration. *Ocean Eng.* **2018**, *167*, 369–379. [CrossRef]
54. Piaggio, B.; Vernengo, G.; Ferrando, M.; Mazzarello, G.; Viviani, M. Submarine Manoeuvrability Design: Traditional Cross-Plane vs. x-Plane Configurations in Intact and Degraded Conditions. *J. Mar. Sci. Eng.* **2022**, *10*, 2014. [CrossRef]
55. Watt, G.; Gerber, A.; Holloway, A. Submarine hydrodynamics studies using computational fluid dynamics. In Proceedings of the CMHSC, Halifax, NS, Canada, 21–22 September 2007.
56. Bettle, M.C. *Baseline Predictions of BB2 Submarine Hydrodynamics for the NATO AVT-301 Collaborative Exercise*; Defence Research and Development Canada: Toronto, ON, Canada, 2018.
57. Pattison, D. *Stability and Control of Submarines: A Review of Design Criteria and Derivative Prediction Techniques*; Admiralty Experiment Works-Haslar: Gosport, South Hampshire, 1975.
58. Pitts, W.C.; Nielsen, J.N.; Kaattari, G.E. *Lift and Center of Pressure of Wing-Body-Tail Combinations at Subsonic, Transonic, and Supersonic Speeds*; Technical Report; US Government Printing Office: Washington, DC, USA, 1957.